








Cataclastic deformation bands affecting alkaline volcanics along an emerged island in oceanic fracture zone: the Paredão Volcano, Trindade Island

Leonardo Mairink Barão^{1*} , Barbara Trzaskos² , Leonardo Evangelista Lagoeiro² ,
Jukka Laukkanen³, Dandara Ataíde Salvador³ , Herick Faust Daufenbach¹ ,
Natália Gauer Pasqualon⁴ , Maria Cristina de Souza², Rodolfo José Angulo² 

Abstract

The presence of deformation bands (DBs) associated with porous volcanoclastic rocks, it is ubiquitous but poorly described. In Trindade Island, the Paredão Volcano's lapilli tuffs are deposited during the Middle Pleistocene, and several deformation bands are associated with conjugate pairs geometry. To analyze the structural geometry and mineral phase of host rocks, we employed a multiscale approach that included regional fracture and geometry studies in the field, microtectonics with a support of scanning electron microscopy (SEM-EDS), and 2D petrophysical properties analysis. The analysis revealed that the deformation bands result from two mechanisms. The first is a granular flow mechanism characterized by grain rotation and matrix reorganization. This mechanism is also associated with fluid flow and matrix zeolitization. The second mechanism is a cataclastic flow marked by crystal fragmentation and the formation of a fine-grained matrix. It is observed that the pre-existence of mineral cleavages and fractures facilitates these mechanisms. The combination of these two mechanisms, driven by fluid flow, leads to the development of cataclastic bands characterized by the loss of porosity, matrix reorganization, and distinct geometric patterns. Those mechanisms are suggested to be developed in a transtensional context related to the Vitória-Trindade Fracture Zone.

KEYWORDS: phillipsite; fluids; lapilli tuff; cataclastic flow; granular flow.

1. INTRODUCTION

Deformation bands (DBs) significantly impact rock porosity, permeability and grain morphology in various geological and tectonic settings (Fossen et al., 2007, 2018; Balsamo et al., 2010; Alikarami et al., 2013; Ballas et al., 2012; Rodrigues et al., 2015), also DBs impact fluid flow, affecting transport capacity (Antonellini & Aydin, 1995; Parry et al., 2004; Medeiros et al., 2010; Okubo et al., 2009; Souza et al., 2021; Berge et al., 2022; Stohler et al., 2022). Extensive research has been carried out on the petrophysical impacts of DBs on the host rocks (HR) (e.g., Antonellini & Aydin, 1995; Shipton et al., 2002; Farrell et al., 2014; Del Sole et al., 2020; Nogueira et al., 2021; Torabi et al., 2021; Silva et al., 2022).

Most of these structures can be found within porous quartz-rich sandstones (Aydin, 1978; Aydin & Johnson, 1978; Antonellini & Aydin, 1995; Zuluaga et al., 2014; Rodrigues et al., 2015; Soliva et al., 2016; Fossen et al., 2018;

Bonato et al., 2022) and carbonate grainstones (Tondi et al., 2006; Cilona et al., 2012; Dimmen et al., 2017; Del Sole & Antonellini, 2019). They can also occur in poorly lithified sandstone (Pizzati et al., 2020; Nicchio et al., 2023). However, DBs are poorly described in volcanoclastic rocks, but are very commonly observed (e.g., Dinwiddie et al., 2012; McGinnis et al., 2009; Wilson et al., 2003, 2021; Cavailhes & Rotevatn, 2018; Chung et al., 2023; Leroy et al., 2023). The first description of these structures in volcanoclastic rocks was made by Wilson et al. (2003), highlighting the influence of hydraulic dynamics on these structures. Other researchers have conducted additional studies in comparable environments to investigate this occurrence further (Dinwiddie et al., 2006; Evans & Bradbury, 2004; McGinnis et al., 2009).

The current understanding of deformation mechanisms and granularity studies in volcanoclastics is limited, and the influence of fabric, cleavage, and interaction with volcanic glassy, fluids, and gas on the DBs is not well understood (e.g., Evans & Bradbury, 2004; Cavailhes & Rotevatn, 2018; Chung et al., 2023). It is recognized that variations in hydrogeology can impact the DBs, affecting the fabric and grain morphology (Dinwiddie et al., 2006, 2012). Furthermore, the volcanic system's contribution can significantly the emplacement of brittle deformation systems, as described by Wilson et al. (2021). The volcanic system can affect the development of DBs and fluid presence, indicating a complex interaction between volcanism and deformation processes. The DBs can be associated with a different tectonic context in compressive settings, displaying both reverse-sense and strike-slip kinematics (Cavailhes & Rotevatn, 2018), as well as in extensive/transtensional settings, demonstrating normal-

¹Universidade Federal do Paraná – UFPR, Programa de Pós-graduação em Geologia, Laboratório de Análise de Bacias – LABAP, Curitiba, PR, Brasil. E-mails: leonardobarao@ufpr.br, herick.fd@gmail.com

²Universidade Federal do Paraná – UFPR, Departamento de Geologia, Programa de Pós-graduação em Geologia, Curitiba, PR, Brasil. E-mails: barbaratzaskos@ufpr.br, leonardo.lagoeiro@ufpr.br, cristinasouza@ufpr.br, angulo@ufpr.br

³Geological Survey of Finland – GTK, Espoo, Southern Finland. E-mails: jukka.laukkanen@gtk.fi, dandara.salvador@gtk.fi

⁴University of Hawai'i at Mānoa, Honolulu, Hawai'i, United States. E-mail: ngp2516@hawaii.edu

*Corresponding author.



sense kinematics (e.g., Dinwiddie et al., 2006; Cavailhes & Rotevatn, 2018; Leroy et al., 2023; Nicchio et al., 2023).

The DBs identified in the stratified lapilli-tuffs of Trindade Island represent structures formed during Pleistocene volcanic activity in transtensional context associated with an oceanic fracture zone, described by Vitória-Trindade Fracture zone developed in a transtensive context (Barão et al., 2020). Therefore, making this area a unique site to study the influence of the fabric and the interaction between volcanic fluids and gases in the formation of DBs in transtensive tectonic regimes.

This paper defines the main structural characteristics of the DBs in porous volcanoclastic rocks formed in Paredão Volcano, Trindade Island. We (i) studied the distribution, geometry, and architecture of DBs in the Paredão volcano, as well as microstructures and the properties of HR and DBs such as porosity data, the difference of deformation in glass and main minerals as feldspar and pyroxene; (ii) define the main deformation mechanisms, mineralogical control on deformation mechanisms and the relationship with tectonics; (iii) discuss the relationship between deformation and the volcanism.

2. GEOLOGICAL CONTEXT

The Trindade Island and Martim Vaz Archipelago emerged portions of the Vitória-Trindade Fracture Zone (VTFZ) with the main direction E-W, which is located roughly 1150 km eastward to the Brazilian coast reaching a width of up to 200 km along the fault (Figure 1A). The VTFZ is associated with the most recent alkaline volcanism in the Brazilian Territory, this zone of weakness allowed magma to rise as the South American plate moved over a mantle anomaly, during Atlantic Ocean formation (Hartnady & Le Roex, 1985; Siebel et al., 2000; Almeida, 2006; Alves et al., 2006, 2022). This made it possible to form volcanoes aligned with the VTFZ, which when emerged appear as islands, when inactive, they end up being eroded by marine and subaerial erosion, transforming into submarine-forming guyots along the VTFZ (Figure 1B) (Sztamari & Mohriak, 1995; Rego et al., 2021). The islands of Trindade and Martin Vaz are the only ones not eroded and emerging from this volcanic chain, denominated Vitória-Trindade Ridge (Figure 1B).

The volcanic activity in Trindade Island has initial age of approximately 3.9 Ma to less than 0.25 Ma (Pires et al., 2016). This volcanic activity is associated with the post-Gondwana breakup and the opening of the South Atlantic (Hawkesworth et al., 1999; Almeida, 2006; Gibson et al., 2006) and is believed to be linked to mantle plume activity (Hartnady & Le Roex, 1985; Siebel et al., 2000).

The tectonic framework of Trindade Island is characterized by a predominant NW–SE structural trend, as evidenced by the orientation of fractures, faults, and dikes in this direction (Almeida, 1961) (Figure 1C). Barão et al. (2020) identified an extensional phase responsible for the formation of normal faults trending NNW–SSE (Figure 1C), associated with a post-volcanic stage. The development of NE marks the subsequent progression of deformation on Trindade Island–SW-striking right-lateral strike-slip faults (Figure 1C).

The structural relationship between the normal and oblique faults suggests that the main shortening direction was initially vertical, indicating active tectonics during the first volcanic phase of the island, suggesting active tectonics during

the first volcanic event of the Island (Barão et al., 2018, 2020; Motoki et al., 2024). Trindade Island's volcanic history dates to the Middle Pliocene and continued until the Pleistocene (Pires et al., 2016). The accumulation of lava formed the island flows, pyroclastic deposits, and phonolitic intrusions from strongly sodic alkaline and SiO_2 under saturated magma (39.8 ± 42.9 wt.%) (Marques et al., 1999; Siebel et al., 2000; Bongioiolo et al., 2015; Monteiro et al., 2022).

Almeida's (1961) defined five units, which were later redefined following the most up-to-date stratigraphic nomenclature (Monteiro et al., 2022; Santos et al., 2025), being them: Trindade Fm., Desejado Fm., and the Morro Vermelho Fm., Valado Fm., and Paredão Volcano Fm. (Figure 1C). The study area corresponds to the most recent volcanic event on Trindade Island (~0.25 Ma; Pires et al., 2016), located on the southeastern edge and known as the Paredão Volcano Formation (Figure 1C). This event resulted in the deposition of a range of pyroclastic components, with a minor contribution from effusive eruptions, as described by Pires et al. (2016). The volcanic edifice associated with this activity is well-preserved and consists of a scoria cone known as Paredão Volcano (Figures 1C, 1D). The volcanic structure exposes the intercalation of lapilli-tuffs, tuff-breccias, breccias, and agglomerates (Pires et al., 2016; Pasqualon et al., 2019) (Figures 1D, 1E).

2.1 Host rock characterization

This study focuses on proximal pyroclastic deposits and associated deformation bands (DBs) cutting through a proximal pyroclastic sequence composed of alternating layers of lapilli-breccias and lapilli-tuffs, characterized by planar bedding, massive textures, and reverse grading (Figures 1D, 1E). These deposits consist of volcanic ash, lapillitic scoria, bombs, and nephelinitic lava blocks (Pasqualon et al., 2019). The volcanic sequence is interpreted as a scoria cone formed primarily by Strombolian eruptions, with subordinate phreatomagmatic activity (Pires et al., 2016; Pasqualon et al., 2019).

According to Pasqualon et al. (2019), the lapilli-tuffs contain Y, P, and X-shaped shards with subangular scoria lapilli fragments, ranging in size from ash to lapilli, with reverse grading and ballistic bombs and blocks. Oxidized olivine phenocrysts occur within scoria fragments, and pores are often partially or fully filled with zeolite. Fine zeolite grains and mineral particles constitute the groundmass. The volcanic layers are locally tilted by fault surfaces that affect the proximal deposits (Figures 1D, 1E). This study emphasizes DBs associated with conjugate normal faults, typically dipping between 45° and 80° , reflecting the influence of transtensional stress on Trindade Island (Barão et al., 2020).

3. METHODS

3.1 Spatial analysis and outcrop characterization

The deformation bands (DBs) and faults were initially characterized using aerial imagery, as these structures are effectively delineated through aerophotogrammetric surveys (Bemis et al., 2014; Bonato et al., 2022; Freitas et al., 2023). A UAV survey provided high-resolution imagery (10 cm resolution; Figure 2A), which was processed, shaded, and interpreted using ArcGIS 10.6.1.

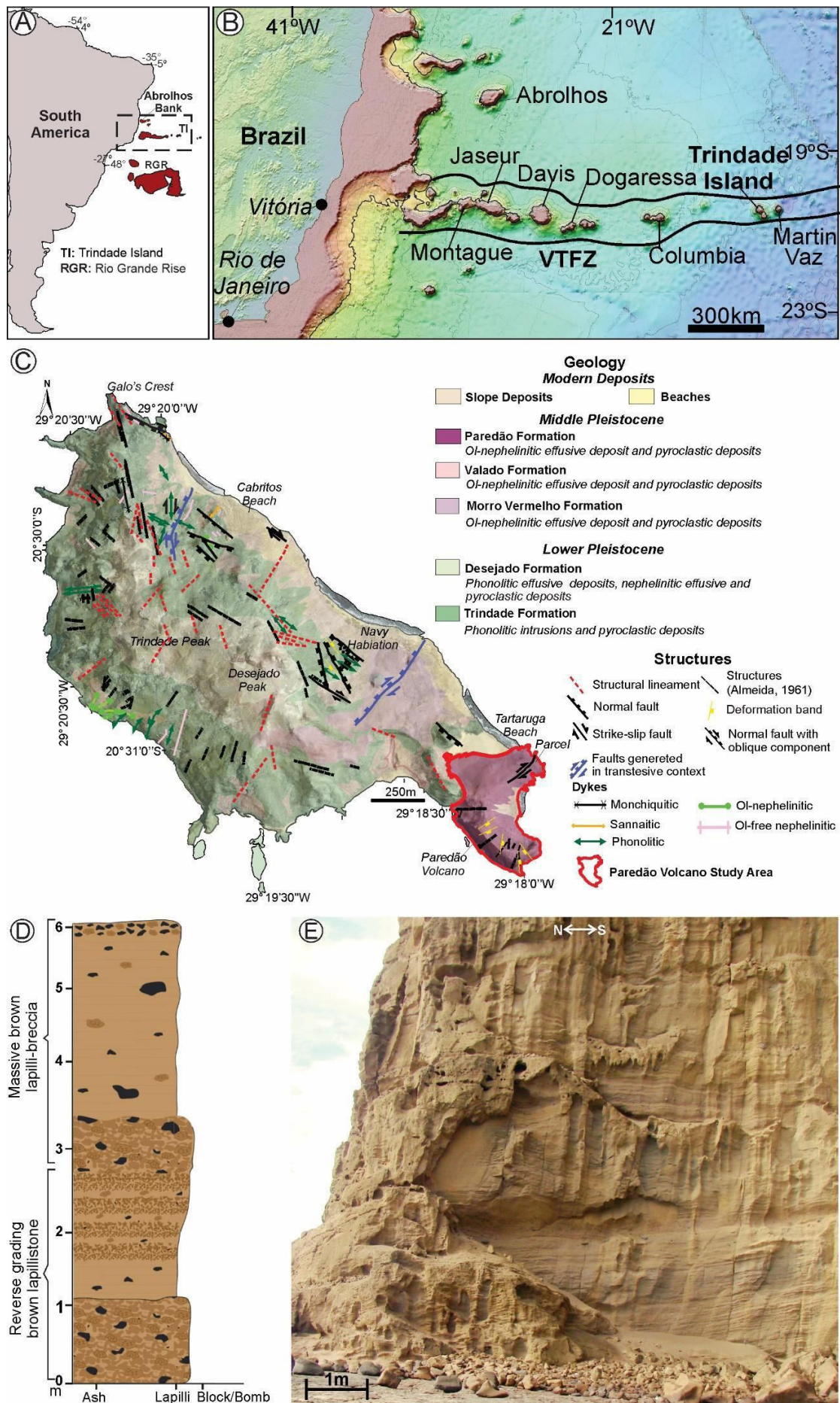


Figure 1. (A) Localization of Trindade Island; (B) location of Trindade Island in the South America comprising the E-W direction Vitória-Trindade Chain; (C) the Island is composed of five distinct geological units with ages varying between Lower Pleistocene to Middle Pleistocene (3.7 to <0.17Ma) (Modified of Barão et al., 2020). The Paredão Volcano is highlighted in the map; (D) stratigraphic column depicting the proximal facies of pyroclastic deposits. adapted from Pasqualon et al. (2019); (E) Image showing the volcanic layering and stratification of the Paredão Volcano.

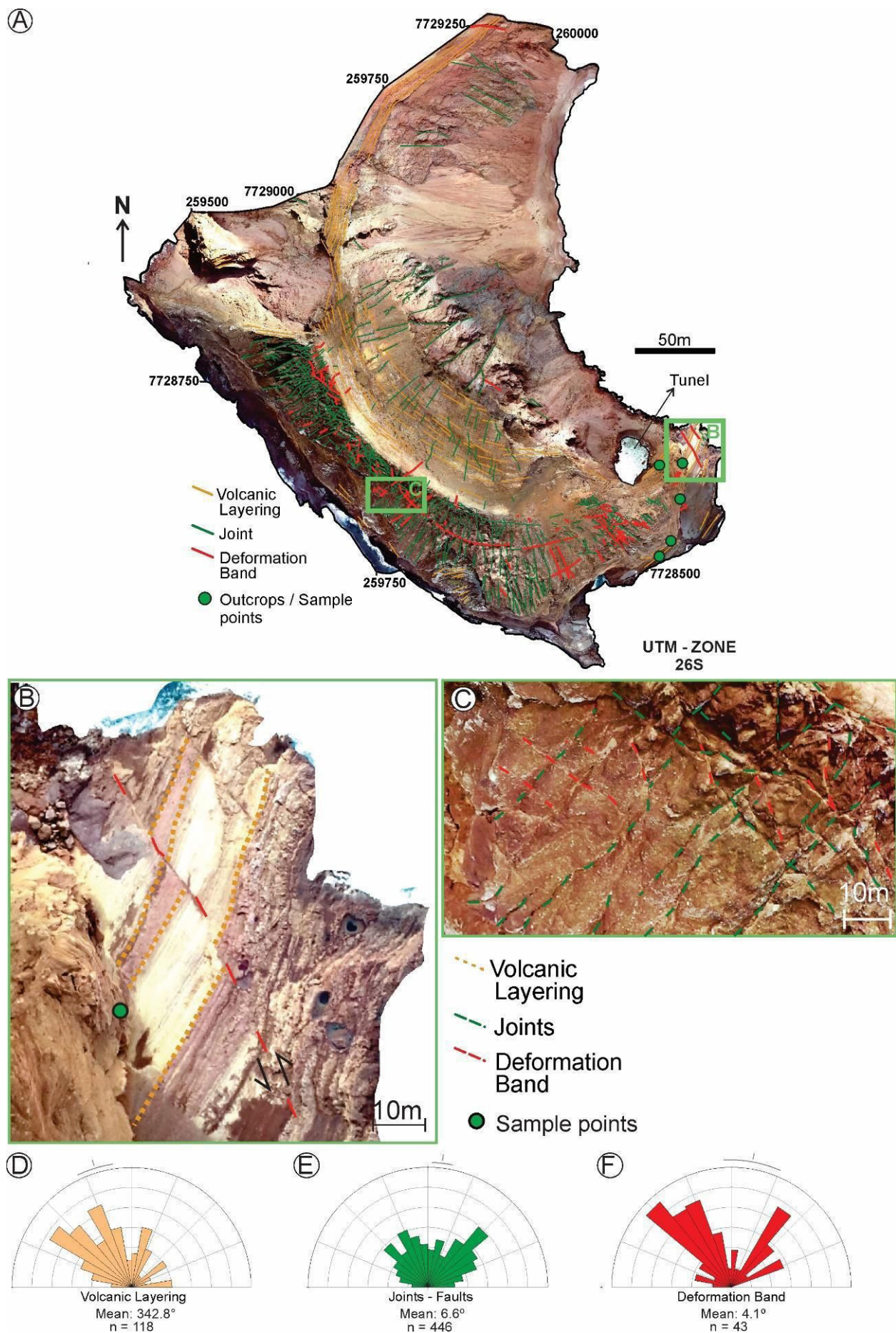


Figure 2. The spatial analysis of the structures observed in the Paredão Formation. (A) A UAV image of the Paredão Volcano, which highlights the main fractures, volcanic layering, and deformation band; (B, C) Interpreted structures in UAV highlighting the joints and Deformation Bands (DBs); (D) rose diagram of volcanic layering; (E) rose diagram of joints; (F) rose diagram of DBs.

The interpretation of linear structures in the UAV images allowed identification of both primary features, such as volcanic layering, and secondary features, such as joints and DBs. Azimuthal orientations were extracted using the Azimuthfinder plugin (Queiroz et al., 2014) for ArcGIS, and directional rosettes were generated with Dips software (Rocscience), enabling detailed structural characterization of the Paredão Volcano (Figure 2A).

Field-based structural analysis involved observing, describing, and mapping five accessible DB outcrops along the Paredão Volcano (Figure 2A). Structural data, including dip and strike, were collected at each site, and photomosaics were constructed to support mapping and sketching. Oriented samples were also collected for laboratory analyses, including petrography, SEM, and EDS studies.

3.2 Microscopic analysis

The samples were analyzed using thin sections to identify the deformation mechanism during DB formation by delineating microstructures, tectonic fabric, compaction, porosity, and mineralogy. Also, observe the alteration of crystals and matrix inside and outside the DBs. We analyzed the porosity of 18 HR and 14 DB samples using the software ImageJ.

3.2.1 ImageJ porosity analysis

ImageJ software differentiates porosity characteristics of deformation bands (DBs) and host rock (HR). To analyze the porosity of both HR and DBs, we used the software ImageJ (Ferreira & Rasband, 2012; Schneider et al., 2012) and followed the methodology employed by Dimmen et al. (2017) and Leroy et al. (2023) for 2D macroporosity analysis of DBs and HR. We chose 300x1200 pixel areas of HR and DBs in thin sections to compare porosity, because it's high quality image can be examined by the software. The porosity was estimated in selected photomicrographs and using a macro developed by Grove & Jerram (2011).

That macro is designed to convert images that are raster, which stands for Red, Green, and Blue, to HSB format, which stands for Hue, Saturation, and Brightness (Grove & Jerram, 2011). This process differs from a red threshold color, therefore, the blue epoxy in the empty spaces from the rest of the matrix color spectrum using a red threshold image is also converted to black and white, resulting in a binary image. This image is then analyzed for "particle" analysis to measure the percentage of porosity and the total area of pores.

3.2.2 SEM-EDS analysis

Samples were analyzed using a Thermo-FEI Quanta 650 SEM equipped with a Mineral Liberation Analyzer (MLA) at GTK for high-resolution porosity and mineralogical characterization. The system, integrated with EDS, enabled mineral chemical analyses, with a thin carbon coating applied to prevent electron charging (Kong et al., 2019).

The XMOD_STD MLA method employed backscattered electron (BSE) imaging to distinguish mineral phases in both host rocks and deformation bands. Mineral identification, porosity mapping, and modal mineralogy determination were based on BSE images and spectral library comparisons (Supplementary Material 1).

Additionally, a Renishaw InVia Qontor Raman microscope was used to differentiate zeolite types (Krolop et al., 2019) (Supplementary Material 2).

4. RESULTS

4.1 Spatial distribution of structures

The circular shape of the Paredão Volcano (Figure 2A) is strongly influenced by fractures, faults, and DBs (Figures 2B, 2C). Four main structural features are distinguishable: volcanic layering and stratification, joints, faults, and DBs (Figure 2A). UAV imagery (Figure 2A) reveals subhorizontal volcanic layers (Figure 1E) with a predominant orientation of N30-50W (Figure 2D).

The eastern portion of the structure has been eroded or collapsed and is no longer accessible (Almeida, 1961). The remaining layers consist of stratified deposits interbedded with lapilli-breccias and lapillistone, as described by Pasqualon et al. (2019) (Figures 1D, 1E). Joints, faults, and DBs are easily distinguishable in UAV images. Joints and faults appear as dark features (Figure 2B) due to voids created by fracturing, while DBs appear brighter (Figure 2C) because of their subtle prominence, as observed in outcrops (Figure 3). Faults and joints are dispersed throughout the analyzed section of the Paredão Volcano, exhibiting a radial pattern associated with cooling and collapse processes (Figure 2E). These structures locally displace volcanic stratification, resulting in offsets ranging from 0.30 to 1.00 m (Figure 2B).

The DBs are oriented along two main directions: N20-45W and N20-30E. In certain areas, they intersect to form conjugate patterns (Figure 3A), which are indicative of localized deformation processes.

4.2 Deformation bands in macroscale

The UAV images and field outcrops reveal mainly two DBs geometries: (i) conjugate patterns of DBs (Figures 3A, 3B) and (ii) isolated DB clusters locally displacing volcanic stratifications (Figures 3C-F).

The conjugate pair geometry consists of structures with scattered orientations (Figures 3A, 3B), moderate to high dip angles (45-75°), and local normal stratigraphic displacements of 3-7 cm. They are sparsely distributed (5-10 m apart) along the Paredão Volcano and are easily identifiable in drone imagery (Figure 2C).

DB clusters exhibit greater displacement, with lapilli-tuff stratifications displaced by 3-10 cm (Figures 3C-F). The thickness of these DBs ranges from 2 to 10 cm. Vertical, newly formed normal faults frequently intersect the DBs (Figure 3C). Eye and ramp structures, formed by two or more sub-parallel deformation band fault segments, are also observed (Figure 3E), highlighting an anastomosed geometry (Mollema & Antonellini, 1996).

Reverse slip is also recognized in the DBs clusters, with reverse faults resembling the conjugate pair morphology and local displacements of 2-3 cm (Figure 3F).

The conjugate pair structures have a mean orientation of approximately N45E and N45W (Figure 3G), with an interplane angle of about 60°. The DB clusters with normal kinematics have a mean orientation ranging from N40°W to N45°W, with dip angles between 30° and 45° (Figure 3H). In contrast, clusters with reverse kinematics exhibit mean orientations ranging from N85°W to N15°E, with dip angles between 40° and 85° (Figure 3I).

4.3 Deformation bands in mesoscale

The DBs are characterized to decrease in grain-size from the HR to the DB. Compared to the HR, DBs are more

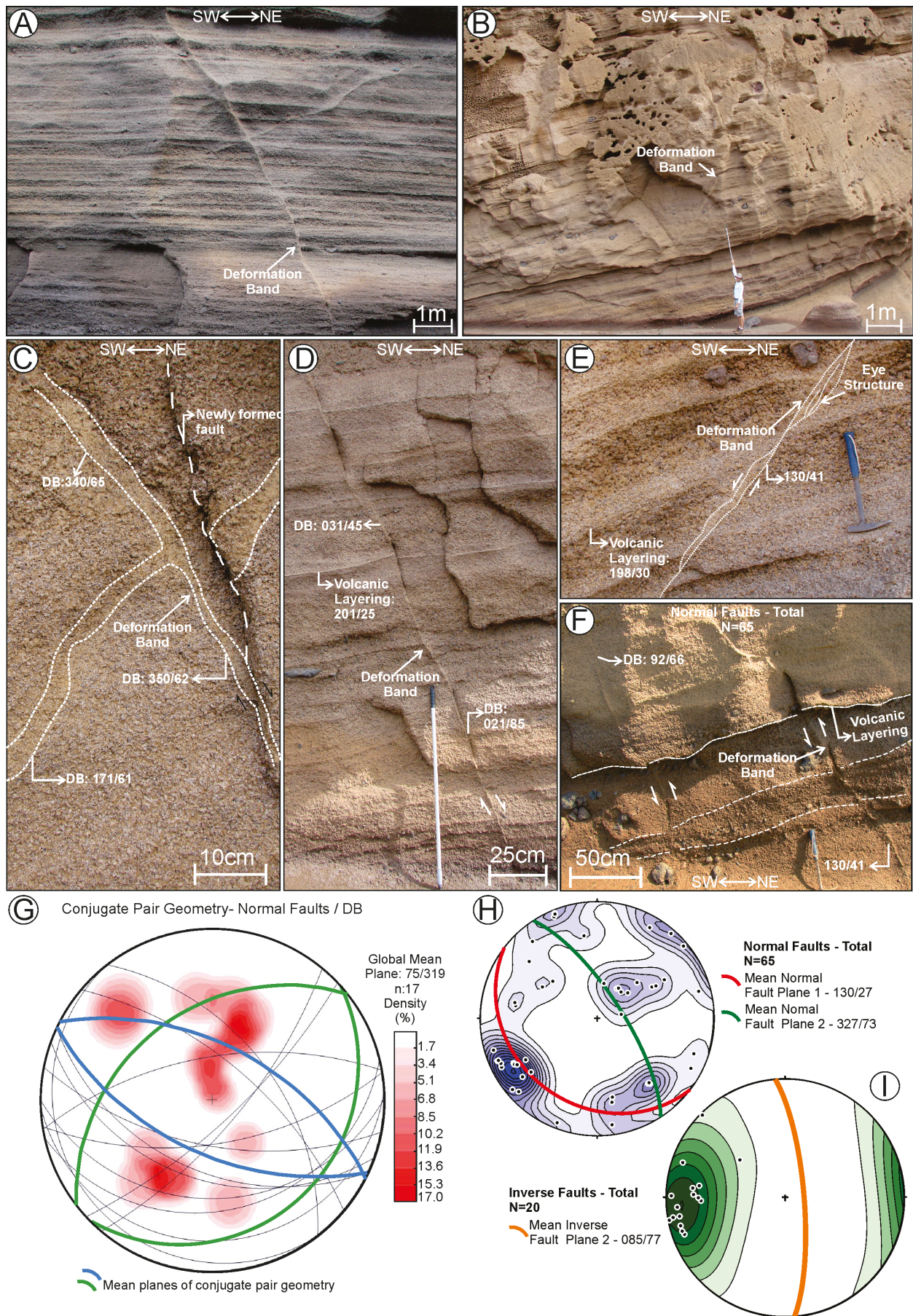


Figure 3. Conjugate pairs geometry of normal faults and deformation bands in the Paredão Volcano. (A, B) Photos of DBs localized in conjugate structures; (C) zoom of conjugate pair geometries with DB; (D) DBs with dimension of (2-3cm) cutting the volcanic stratification with displacement causing the displacement of 5-10cm with normal kinematics; (E) the eye structure formed by joining different fault planes; (F) DBs causing a local inverse displacement (about 3cm); (G) equal-area projection of conjugate faults associated with a dihedral angle between planes around 60°. blue and green planes indicate de mean values for the conjugate pair; (H) equal-area projection of deformation bands planes with normal kinematic; (I) equal-area projection of deformation bands planes with reverse kinematic.

densely compacted and have lower porosity (Figure 4). Internally, DBs show a structural fabric that involves fragmentation or cataclasis of minerals and lithoclasts, decrease the grain size, and reduction of pore size and its complete closure along the bands (Figures 4A, 4C, 4E). Three distinct zones can be observed within the DB: the main damage zone where is observed the DB, the interband space (IS), which extends approximately 3 to 5 mm from the main damage zone, and the preserved HR (Figures 4B, 4D, 4F).

Due to fault displacement, grains and fragments within the DBs have been rotated and reoriented, forming structures resembling pressure shadows (Figures 4A and 4B). The fragments exhibit a finer-grained matrix asymmetrically arranged around angular-shaped fragments, which appear as gray-colored areas (Figures 4A and 4B).

Angular minerals and glass fragments shows slightly preferred oriented shear planes, with matching normal shear sense observed in DBs outcrop (Figures 4E, 4F). The fabric generated during the shearing propitiate the orientation

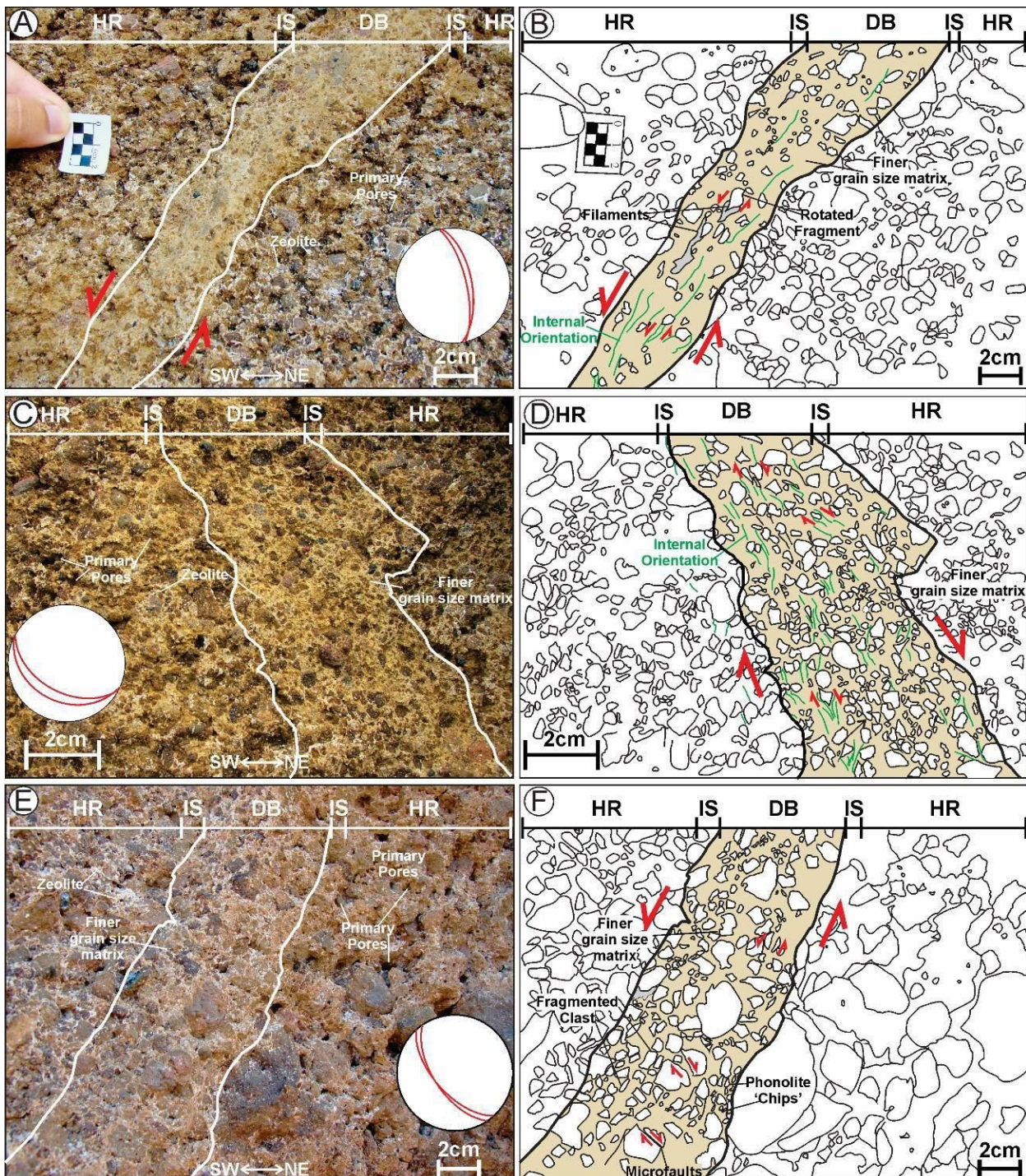


Figure 4. Enlargement (or details) of the internal structures observed in the deformation bands and the zonation of the deformation bands (DBs) in outcrop. (A, B) It is possible to observe the internal orientation, the matrix reduction; (C, D) irregular morphology of DBs, with fine grained matrix and some internal orientation; (E, F) microfaults with local displacement of the clasts, with similar kinematic to DB. HR: Host Rock; IS: Interband Space; DB: Deformation Band.

intern of the DBs (Figures 4A to 4F).

Another characteristic that distinguishes the DBs from the HR is the presence of cement within the bands (Figure 4). The bands are predominantly composite by finer grain size matrix (Figures 5A to 5D). In some cases, a whitish mineral can be observed filling the pores, probably corresponding to a zeolite. (Figure 4C). In the HR, cavities produced by gas escape during

formation can be observed as primary pores (Figure 4), whereas, in the DBs, these structures are sealed by light grey cement composite by zeolite and a finer grain size matrix (Figures 4A, 4C, 4D).

4.4 Deformation bands in microscale

The thin sections revealed a mineral assemblage mainly consisting of pyroxene (5-35%), K-Feldspar (5-20%),

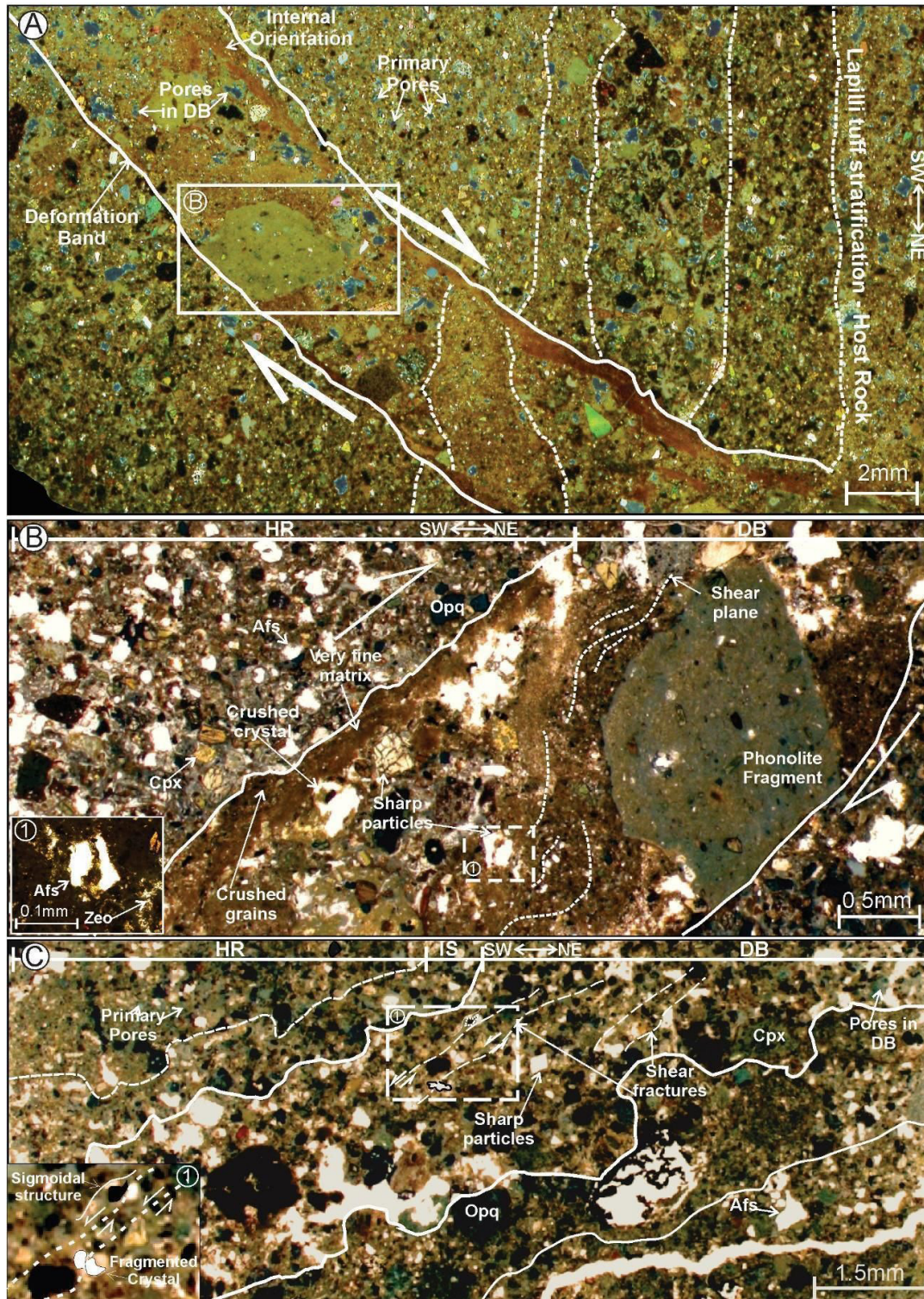


Figure 5. (A) Scanned thin section of the host rock (HR) and the deformation band (DB), where we can see the local displacement of volcanic stratification with 2mm; (B) zoom area of deformation, highlighting the presence of pressure shadow around the phonolite fragment and the fine-grained matrix generated by cataclastic and comminution process. It also observes the weak orientation in the matrix; (C) clearly defined deformation band zones characterized by grain size reduction and matrix deformation within the region. Additionally, shear fractures can be observed running parallel to the walls of the deformation bands, exhibiting kinematics similar to those indicated by crystal sigmoidal opaque shape. Opq: Opaque mineral; Cpx: Clinopyroxene; Afs: Alkali Feldspar; HR: Host Rock; IS: Interband Space.

amphibole (5-15%), spinel (5-10%), volcanic glass (5-10%), zeolite in cavities and matrix (5-20%), glass (5%), and magnetite (traces) (Figure 5A). This assemblage likely represents the lapilli tuff described by Pasqualon et al. (2019).

The petrographic sections (Figure 5) shows that the DBs have irregularly shaped mineral grains and rock fragments scattered randomly in a cohesive matrix with reddish colors (Figure 5A). Fragments observed in the DBs are lack distinct optical microstructures and exhibit a roughly equant shape (Figure 5A). Grain aggregates in the matrix show no specific orientation and display variability in shape and size (Figure 5B). Two distinct types of interactions between the HR and DB can be observed, resulting in different morphologies. These include the presence of an interband space (Figures 5A-E) and transitional features ranging from protocataclastic to ultracataclastic textures, which are observed in some fractured crystals and a fine-grained matrix (Figures 5A-E).

The scanned thin section of the DBs reveals a local displacement of HR stratification (approximately 2 mm), with the internal stratification being much finer, more disorganized, and fragmented compared to the HR. The mineralogy of the DBs consists of fragmented minerals, phonolite clasts, and a finer-grained matrix (Figure 5A).

DBs matrix shows fewer internal pores when compared to HR (Figures 5B and 5C), with the pores are generally filled by a fine-grained matrix or sealed by deformational or zeolitization process (Figure 5B and 5C). It exhibits a cataclastic texture fabric dominated by comminution and fragmentation, resulting in small, sharp particles of K-feldspar and clinopyroxenes (<1 mm) (Figures 5B and 5C). As observed in macrostructures (Figure 4A and 4B), pressure shadow microstructures occasionally form around large fragments of phonolites (Figure 5B). These structures indicate normal kinematics similar to those observed in the field. Additionally, the internal shearing generate shear surfaces, resulting in matrix orientation (Figure 5B).

The shear fractures observed within the DBs have the same sense of shear as the overall DBs (Figure 5C). These fractures can cut across fragments of feldspar grains, which indicates the deformation occurred within the DBs. Microscopic deformation may occur at specific layers where cataclasis dominates.

4.5 2D porosity and SEM analysis

In the HR samples, porosity appears as rounded cavities ranging from 50 to 400 μm (Figure 6A). The photomicrographs reveal low connectivity between pores in the HR (Figures 6A), with an average porosity of approximately 16%. However, when fractures are more densely distributed in the HR samples, porosity can increase to up to 40%.

DBs samples exhibit reduced porosity, with only a few open spaces remaining unfilled due to mineral precipitation or compaction (Figure 6B). The DBs have a porosity of up to 13%, with an average of 6% along the band (Figure 6C). At this study scale, the pores in the DBs are isolated and lack connectivity. Unlike the rounded pores observed in the HR samples, the pores in the DBs appear elongated or rectangular, without any specific orientation.

The microstructures of the DB are different from those of the HR samples, as observed in SEM images (Figure 7). The grains in the DBs are visually smaller than HR (Figure 7A - 7D), and some exhibit micro faults and

shearing features (Figure 7D). The porosity and pore sizes in the DBs are lower than those in the HR samples. However, it is essential to note that all analyses were conducted on thin sections, and some of the observed porosity may be due to artifacts rather than actual pores. This is because SEM characterization has limitations in revealing the morphology of pores in three dimensions.

Some grains in DBs exhibit rounded contours (Figure 7D), it is embedded in a finer-grained matrix that contains fragments distributed without preferential orientation. Approximately 63% of the DB comprises of the finer-grained cataclastic matrix, while the rest is fragments of zeolite, pyroxene, k-feldspar, amphibole, and oxides, similar to HR. The groundmass in the DBs is classified as a finer-grained matrix in SEM-EDS analysis (Figure 7A and 7B) since these grains are too fine to be detected.

There is a significant difference in the occurrence of phillipsite, a type of zeolite, is observed in the DBs and HR samples (Figures 8A and 8B). In the DBs, phillipsite appears fragmented, while in the HR samples, it remains undeformed, preserving its fibrous morphology and, in some cases, filling cavities. Additionally, flat and prism-shaped minerals, such as mica and amphibole, are aligned with their longest dimensions parallel to the DB walls. Tiny fragmented grains surround larger ones, transitioning from protocataclastic to ultracataclastic textures in certain portions of the DBs (Figure 8C). The ultracataclastic texture exhibits intense deformation, with shear planes forming parallel to the DB orientation (Figure 8C). In contrast, the cataclastic texture is characterized by partial orientation and rotation of fragments embedded in a finer-grained matrix (Figure 8D).

The presence of biotite with deformed cleavage, suggests normal kinematics within the DB (Figure 8E) and highlights the mechanical incorporation of larger fragments. The protocataclastic texture demonstrates pervasive fragmentation and significant grain size reduction (Figures 8E and 8F), with flaking most pronounced on K-feldspar, phillipsite, and pyroxene grains. Rotated grains (Figure 8E), as well as wing cracks and fractures exploiting mineral cleavage (Figure 8F), are commonly observed.

4.6 Grain size distribution

We compare the histograms of grain size distribution between HRs and DBs, it becomes evident that there is a reduction in grain size. We analyzed the grain size distributions of pyroxene and feldspar, the most abundant grains in HR and DB. The data presented in Figure 9 and in Tables 1 to 3 represent the grain size distribution information for pyroxene and feldspar in HR and DB.

The tendency curve in HR shows particle sizes mostly between 45 and 100 μm (Figure 9A). The mean grain size for pyroxene is approximately 218 μm with a standard deviation of 270 μm .

In contrast, the grain sizes of pyroxene and K-feldspar in DB are significantly smaller ($\geq 5 \mu\text{m}$), with the largest size being around 100 μm (Figure 9C-9D). The average length of pyroxene is about 30 μm with a standard deviation of 48 μm (Figure 9C). For K-feldspar, they exhibit a similar statistical trend with an average size of 35 μm and a standard deviation of about 52 μm (Figure 9D).

The trend of size reduction persists even when the two minerals are combined, considering their particle

Table 1. Mineral contents data for the analyzed thin section.

Mineral	Area 1 - Host Rock (Wt%)	Area 2 - Deformation Band (Wt%)
Quartz	0.01	0
Pyroxene	15.42	9.04
Amphibole	11.76	6.73
K_feldspar	5.38	3.83
Albite	0.08	0.01
Biotite	5.23	6.33
Phillipsite_Ca_K	13.08	5.89
Titanite	0.49	0.62
Apatite	0.82	0.52
Magnetite_Ti	4.52	2.63
Ilmenite	0.45	0.25
Pyrrhotite	0	0
Pyrite	0	0
Glass	0.62	0.51
Groundmass	41.57	63.29
Unclassified	0.57	0.34
Total	100	100
Number of measured points	28506	8825

Table 2. Grain size distribution in deformation bands and host rock for Pyroxene.

Mineral Size Distribution - Grain Layer - SEM			
Size	Particle Count	Retained W (%)	Cumulation Passing Wt (%)
1009.08	0.00	0	100.00%
848.53	1.00	1.05	98.95%
713.52	0.00	0	98.95%
600	2.00	1.02	97.93%
504.54	3.00	1.2	96.73%
424.26	14.00	3.67	93.05%
356.76	23.00	4.25	88.80%
300	38.00	4.98	83.82%
252.27	57.00	5.47	78.35%
212.13	113.00	7.45	70.91%
178.38	177.00	8.23	62.68%
150	230.00	7.7	54.97%
126.13	333.00	7.92	47.06%
106.07	455.00	7.63	39.43%
89.19	544.00	6.45	32.98%
75	731.00	6.1	26.88%
63.07	957.00	5.65	21.23%
53.03	1215.00	5.08	16.15%
44.6	1323.00	3.91	12.24%
37.5	1505.00	3.16	9.08%
31.53	1709.00	2.54	6.54%
26.52	1781.00	1.86	4.68%
22.3	1860.00	1.37	3.31%
18.75	1894.00	0.98	2.33%
15.77	2085.00	0.75	1.58%
13.26	1871.00	0.48	1.09%
11.15	3090.00	0.55	5.40%
9.38	1476.00	0.19	3.50%
7.88	3786.00	0.35	0.00%

sizes (Figure 9E-9F). This trend further emphasizes a significant textural alteration between the HR and DB. A closer examination of particle sizes in the HR reveals a normal distribution with a peak between 10 μm and 45 μm , extending up to 600 μm for the largest particles (Figure 9E).

Table 3. Grain size distribution in bands and host rock for Alkaline Feldspar.

Mineral Size Distribution - Grain Layer - SEM			
Size	Particle Count	Retained W	Cumulation Passing Wt (%)
1200	1.00	16.73	83.27
1009.08	0.00	0	83.27
848.53	0.00	0	83.27
713.52	2.00	2.08	81.19
600.00	1.00	0.69	80.50
504.54	5.00	2.77	77.73
424.26	4.00	1.58	76.15
356.76	12.00	3.44	72.70
300.00	13.00	2.67	70.04
252.27	21.00	2.9	67.13
212.13	45.00	4.42	62.71
178.33	67.00	4.74	57.97
150.00	83.00	4.14	53.82
126.13	154.00	5.41	48.42
106.07	189.00	4.71	43.71
89.19	307.00	5.4	38.31
75.00	438.00	5.5	32.80
63.07	636.00	5.66	27.14
53.03	924.00	5.78	21.48
44.60	1120.00	4.97	16.39
37.50	1365.00	4.31	12.08
31.53	1402.00	3.12	8.96
26.52	1517.00	2.38	6.58
22.30	1576.00	1.73	4.85
18.75	1673.00	1.29	3.55
15.77	1989.00	1.07	2.48
13.26	1902.00	0.74	1.74
11.15	3224.00	0.87	0.87
9.38	1516.00	0.3	0.58
7.88	4196	0.58	-

In contrast, in the DB, the trend line varies throughout the graph (Figure 9F 13F), indicating an irregular distribution of grain sizes, with a predominant range of 5 to 10 μm .

5. DISCUSSIONS

The deformational evolution of the Paredão Volcano is driven by the interaction of five key processes: (1) volcanism (Figure 10A), (2) hydrothermalism and mineral alteration (Figure 10B), (3) fracturing assisted by fluid flow and mineral alteration, (4) granular flow, and (5) cataclastic flow (Figure 10C). The Figure 10 summarizes the processes driving the deformation and evolution of the volcano's geological structure. The observed DBs can be classified as cataclastic shear bands (CSBs), as defined by Ballas et al. (2012), in which cataclasis and grain-crushing processes dominate. This is similar to what occurs in immature sandstones or poorly lithified sandstones with a wide mineralogical variety and granulometry, as described by various studies (Aydin, 1978; Chuhan et al., 2002; Rawling & Goodwin, 2003; Fossen et al., 2007, 2018; Exner & Tschegg, 2012; Torabi, 2014; Pizzati et al., 2020; Souza et al., 2021; Nogueira et al., 2021; Silva et al., 2022; Chung et al., 2023).

The main deformation zone (Figure 8A) is characterized by a preferential cataclastic flow orientation, dominated by cataclastic to ultracataclastic textures (Figure 8C). This feature is also evident near the core of the deformation zone, where a

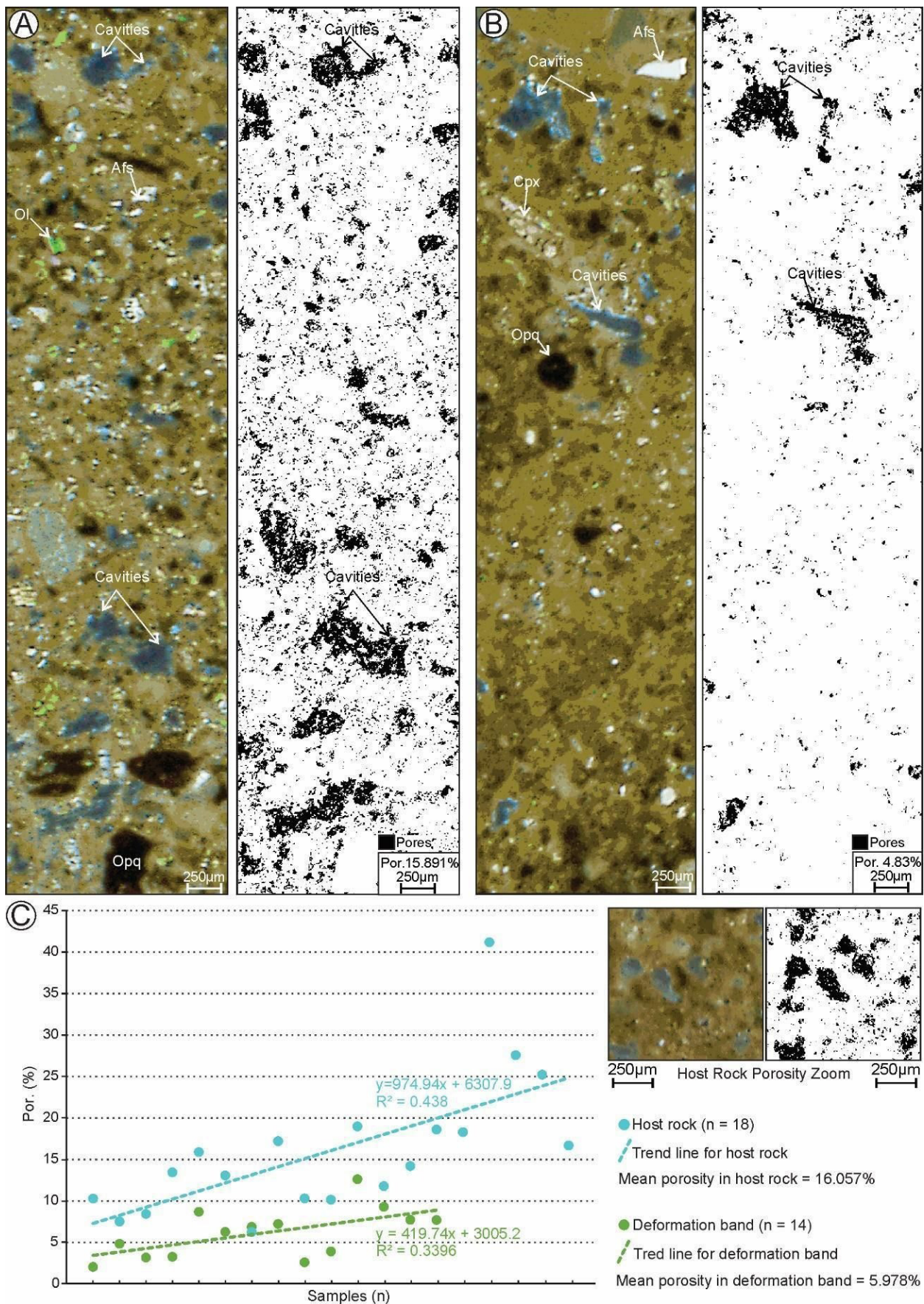


Figure 6. Porosity analysis used photomicrographs and JPor. (A) A photomicrograph of the host rock (HR) was taken, and the HSB macro was applied to estimate the 2D porosity. The porosity in this portion of the HR was estimated at 16%. (B) deformation band was analyzed using the HSB macro, revealing a significant porosity reduction compared to the host rock, with an estimated porosity of 4%; (C) comparative graph was generated, illustrating the variation in porosity between the host rock and the deformation band. The HR exhibited porosity ranging from 7% to 25%, while the deformation band showed porosity ranging from 2% to 11%. Afs: Alkali Feldspar; Ol: Olivine; Opq: Opaque mineral; Cpx: Clinopyroxene.

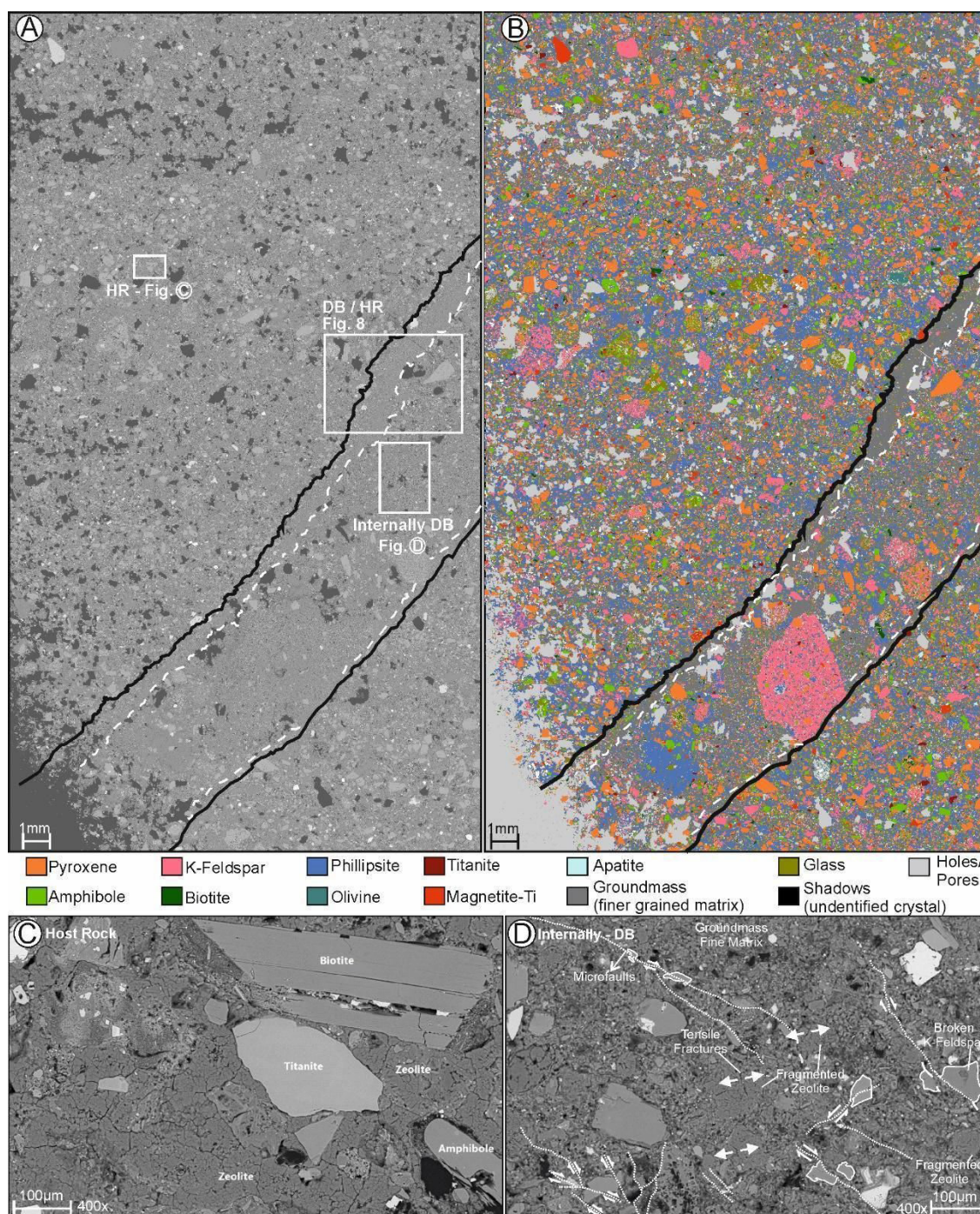


Figure 7. Scanning Electron Microscope (SEM) Backscatter Electron (BEI) and Energy-Dispersive X-ray Spectroscopy (EDS) images were obtained to analyze the textural and mineralogical characteristics of the thin section. (A) The BEI image shows the textural differences between the host rock (HR) and the deformation band (DB). The contrasting features between these two regions are evident; (B) EDS phase map provides mineral identification and highlights the tuffaceous matrix present in the sample. Different minerals can be distinguished based on their elemental composition; (C) zoomed-in image of the HR reveals well-shaped biotite, titanite, and zeolite (phillipsite). These minerals exhibit distinct morphologies and can be identified based on their characteristic composition; (D) the internal portion of the DB is depicted, where the dominant features include groundmass and fragmented crystals. Tensile fractures and microfaults are also observed within this zone.

protocataclastic texture is observed, along with grain alignment and the development of shear fractures (Figures 8C, 8E and 8F). This orientation leads to a local shear planes, likely resulting from intense cataclasis, which accommodates displacement along the direction of the DBs (Cladouhos, 1999; Del Sole & Antonellini, 2019; Pizzati et al., 2020).

Two primary mechanisms govern the deformation process: (i) granular flow, extensively studied by Adam et al. (2005) and further examined by Fossen et al. (2007, 2018) (Figure 10B), and (ii) cataclastic deformation, as described

by Aydin (1978) and Pizzati et al. (2020) (Figure 10C). These studies suggest that initial mineral anisotropy in the host rock, such as cleavage planes, likely facilitated the onset of deformation processes (Nicchio et al., 2018; Cavailhes & Rotevatn, 2018; Souza et al., 2021; Leroy et al., 2023).

5.1 Fluid flow and volcano-tectonic history

The first phase of the geological evolution of the area is represented by the volcanic system involving phreatomagmatic, Strombolian, and Hawaiian eruptions, resulting in flat, layered

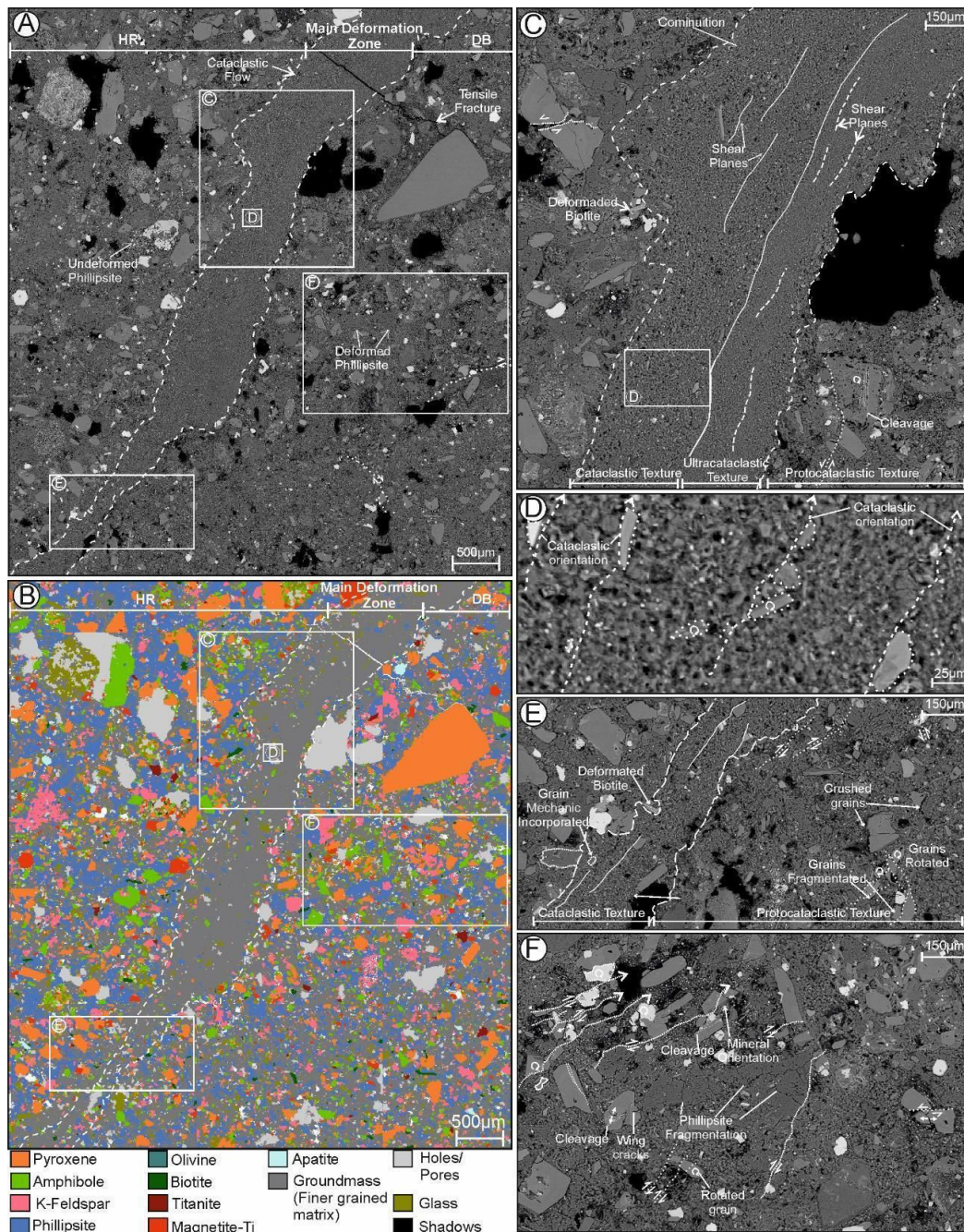


Figure 8. Details of the deformation band are revealed through SEM backscatter images and the EDS phase map. (A) The morphology of the deformation band is prominently displayed, showcasing the main zone of deformation with a distinct texture characterized by intense comminution and fragmentation; (B) EDS phase map allows for the identification of the groundmass. It should be noted that some grains may appear smaller than the detection limit of the EDS, resulting in a gray coloration; (C) Closer examination of the main deformation zone reveals intense cataclastic features and notable matrix reduction. Shear planes are locally associated with mineral alignment, while intragranular and transgranular fractures indicate shearing and deformation. Deformed cleavage is also observed in biotite crystals, further confirming the shearing kinematics; (D) prismatic and phyllosilicate crystal fragments exhibit an orientation parallel to the direction of the deformation band; (E) the mineral orientation within the deformation band becomes more pronounced, with evidence of grain rotation and fragmentation of phillipsite crystals; (F) fragmentation and rotation of grains are evident, suggesting mechanical incorporation within the deformation band.

pyroclastic deposits and lava flows (Figure 10A). These deposits, composed of lapillitic scoria, volcanic ash and lava flows (Figures 1D and 1E) (Pires et al., 2016; Pasqualon et al., 2019).

This second evolutionary phase is marked by the development of pervasive radial fractures, particularly around the Paredão Volcano. This fracturing is associated with volcanic collapse and an extensional stress regime oriented NW–SE, imposed by the VTFZ during volcanic activity (Barão et al., 2020) (Figure 10B). These fractures exhibit a radial pattern centered on the volcanic caldera and are interpreted as tectonically influenced (e.g., De

Rita et al., 1983, Gudmundsson, 2006, Cimarelli & De Rita, 2006; Norini et al., 2019). The fracturing process facilitated hydrothermal alteration of the lapilli-tuff through interaction with magmatic fluids and seawater (Godelistas et al., 2010), creating preferential pathways for fluid circulation (Wilson et al., 2003). As a result of this alteration, volcanic glass and K-feldspar were extensively replaced by phillipsite (Figures 7, 8).

The mineral transformations occurred along stratification planes and fractures (Figure 10B) during hydrothermal or post-depositional phases. These transformations were driven

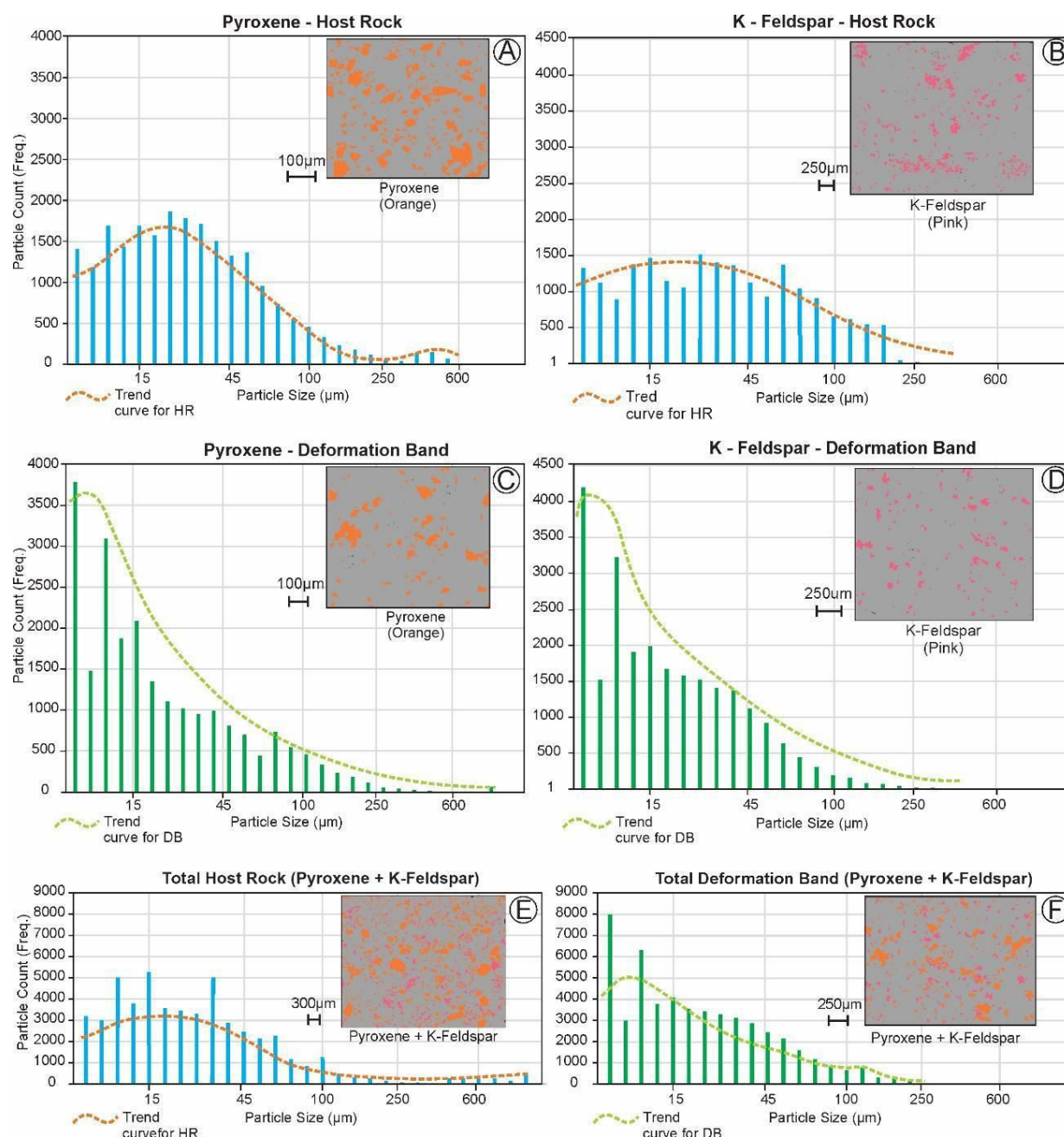


Figure 9. Grain size distribution for Pyroxene and K-Feldspar was obtained using the EDS phase map. (A, B) The grain size distribution of Pyroxene and K-Feldspar in the host rock (HR) reveals a concentration of particle sizes between 15 to 45 μm , indicating a relatively uniform distribution within this range; (C, D) In contrast, the grain size distribution of Pyroxene and K-Feldspar in the deformation band (DB) demonstrates a concentration of particle sizes smaller than 15 μm . This indicates a significant reduction in grain size within the (DB) compared to the HR, likely attributed to the intense comminution and fragmentation; (E) particle size distribution graph for Pyroxene and K-Feldspar in the HR confirms the concentration of particle sizes between 15 to 45 μm , with a relatively symmetrical distribution; (F) particle size distribution graph for Pyroxene and K-Feldspar in the DB highlights the predominance of smaller particle sizes.

by fluid alkalinity, pH variations, alkaline earth element activity, temperature, and pressure, resulting in diagenetic rock alteration (Hay, 1977; Christidis, 2001; Leroy et al., 2023). In case of Paredão Volcano two distinct processes led to the hydrothermalism event. Firstly, the formation of zeolite phillipsite is closely associated with hydrothermal processes. Secondly, the formation of phillipsite is primarily influenced by weathering conditions, especially seawater interaction. Seawater alters pH and temperature, driving the zeolitization of K-feldspar and volcanic glass, resulting in a phillipsite-rich matrix (Hernandez et al., 1993; Robert & Goffé, 1993; Ghiara & Petti, 1996; Etame et al., 2012; Mateus et al., 2020).

The final phase is associated with the development of transtensional tectonics during the Middle Pleistocene, linked to the right-lateral kinematics of the VTFZ, as discussed by Ferrari & Riccomini (1999), Ribeiro et al. (2019), and Barão et al. (2020) (Figure 10C).

The fabric, characterized by the flat arrangement of layers composed of dense lapilli-breccias and lapilli-tuffs, is comparable to cataclastic bands observed in arkosic sandstones or grainstones (Del Sole & Antonellini, 2019; Nogueira et al., 2021; Pizzati et al., 2020; Souza et al., 2021, 2022). These DBs show variations in grain size and mineral composition, reflecting distinct deformational behaviors.

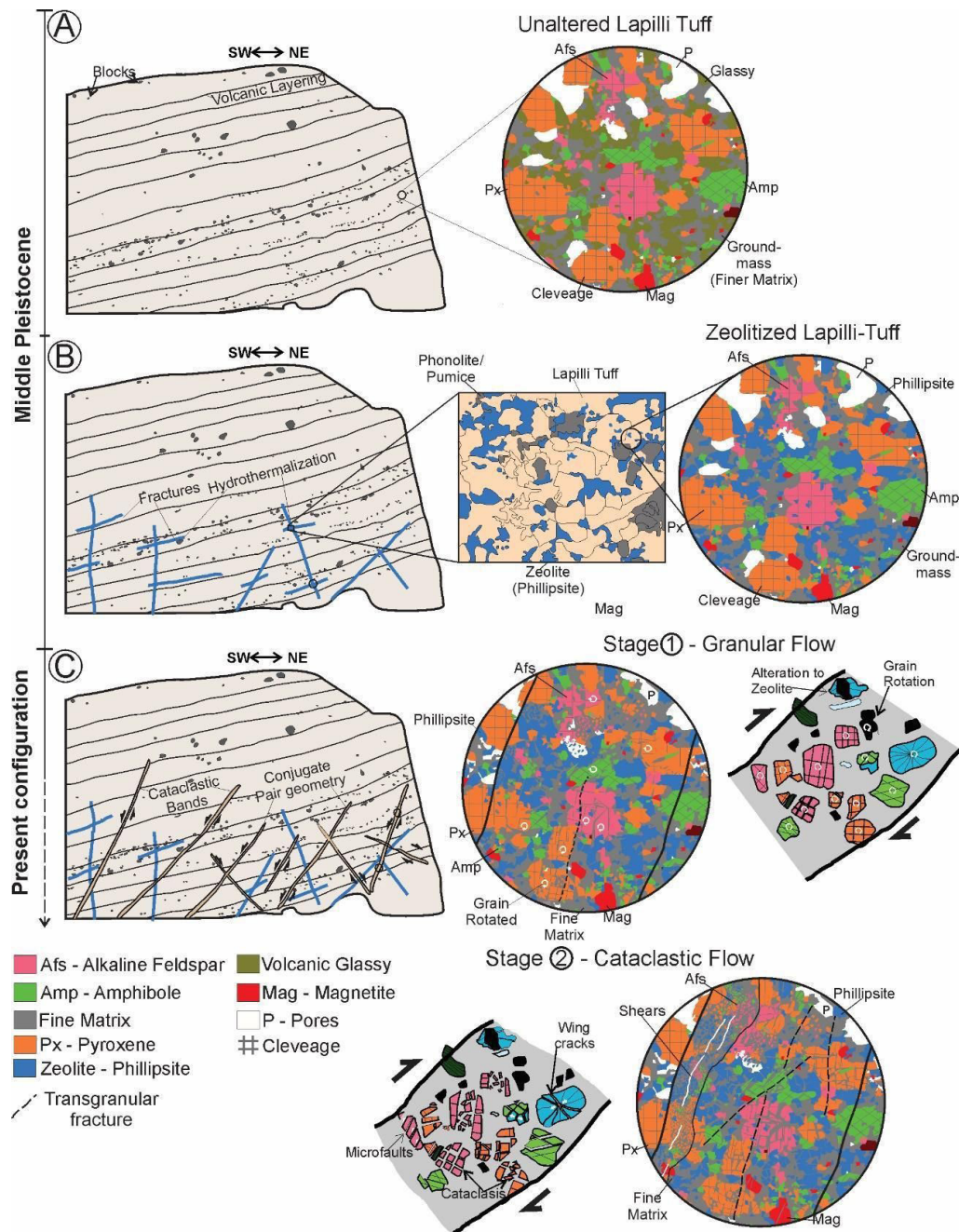


Figure 10. Schematic evolution of the hydrothermal and deformation stages of the Paredão Volcano. (A) The first stage represents the volcanic event, characterized by the deposition of planar stratified pyroclastic deposits and lava flows. The resulting lapilli-tuff facies consists of fragments of pyroxene, alkali feldspar, amphibole, glass, and magnetite. This volcanic activity contributes to the initial stratigraphy and composition of the volcano; (B) the second stage is marked by hydraulic fracturing, which leads to hydrothermal alteration. Fractures created during this process facilitate the circulation of fluids, resulting in the transformation of volcanic glass and alkali feldspar into phillipsite. This hydrothermal alteration is an important factor in modifying the mineralogy of the rocks; (C) the third stage is associated with tectonic activity and the formation of cataclastic bands. This stage can be divided into two sub-stages: (1) the granular flow of particles, where grain rotation and local reorganization occur, resulting in a reduction in grain sizes and the creation of a cataclastic matrix; (2) the cataclastic flow, which involves intense deformation and fragmentation of grains. Cataclastic flow leads to the generation of a very-fine matrix. This stage is a result of the tectonic stress acting on the volcano, leading to deformation.

The deformation process initiates with the fracturing of minerals along pre-existing mechanical weaknesses zones, such as cleavages (Cavailhes & Rotevatn, 2018; Fossen et al., 2018; Souza et al., 2021, 2022) and by grain size effect (Chung et al., 2023). The fracturing induced by the cleavages leads to granular flow, culminating in the complete cataclasis of DBs (Figure 10C). This fracture also induced by the grains size variation, the large particles size results in larger contact forces (Antonellini & Aydin, 1995), impacting in grain fracturing and DB development (Chung et al., 2023).

5.2 Deformation mechanisms

5.2.1 Granular flow

The movement of grains occurs in non-fractured areas, leading to rotation and localized reorganization of primary microstructures (Figures 8D, 8E). The rotational movement produces angular fragments and decreases the porosity in certain regions (Fossen et al., 2018; Pizzati et al., 2020). Grain rotation is more likely to occur along mineral cleavages (Figure 8E). This

deformation process is closely linked to the abundance of minerals like pyroxene, K-feldspar, and amphibole, which enable rotation along the significant cleavage planes (Figure 8F) (Mair et al., 2002; Del Sole & Antonellini, 2019; Cavailhes & Rotevatn, 2018; Pizzati et al., 2020; Leroy et al., 2023). In this case, pyroxene and phonolite appear to be more resistant to the deformation process during granular flow compared to K-feldspar and phillipsite, with pyroxene crystals showing greater resistance to applied deformation (Ulrich et al., 2020; Speciale et al., 2022). The process of granular flow may be influenced by fluid flow resulting from ongoing magmatic activity during deformation or variations in the hydrogeological/hydrological context (Bense & Van Balen, 2004; Wilson et al., 2006; Dinwiddie et al., 2012; Pizzati et al., 2020).

As the area is surrounded by ocean water, there is a potential for interaction between seawater and the rocks of the Paredão Volcano region, under conditions of low temperature (80–100 °C) and pressure (Ramalho et al., 2013; Valdivia, 2022). The finer-grained matrix in both DBs and HR, primarily composed of hydrothermal zeolite (Figures 8, 9), exhibits evidence of contributions from magmatic activity and fluctuations in seawater levels.

Fluid flow is more intense along the DBs than in the HR, likely facilitated by the structures observed in the Paredão volcano. These structures promote fluid flow, possibly associated with a vadose zone where fluids become supersaturated through seawater evaporation (Wilson et al., 2003; Leroy et al., 2023) (Figures 2, 3). However, variations in the vadose zone in this context consider the tropical and humid climate of an oceanic island, which could have directly influenced the control of this zone during the Middle Pleistocene (Jha et al., 2019).

Due to the effects of fluid interaction the grains tend to redistribute, decreasing porosity when comparing the DBs and HR (Figure 6). In the case of DBs, porosity reduction occurs due to fluid circulation along these bands and their interaction with mineral and rock fragments. (Parry et al., 2004; Dimmen et al., 2017). The interaction between fluids and minerals changes pyroxenes, volcanic glass, amphiboles, and K-feldspar, leading to the formation of zeolite cement within these DBs (Figures 7 and 8). This deformation and fluid flow interaction process has likely contributed to the sealing of primary porosity in lapilli-tuff. According to Parry et al. (2004), the chemical alteration process probably played a crucial role in initiating and facilitating the deformation process.

5.2.2 Cataclastic flow

The cataclastic flow can be synchronous to granular flow as described in bibliography (e.g. Pizzati et al., 2020; Leroy et al., 2023). It is characterized by crystal fragmentation and the formation of a finer matrix in the main deformation zone, resulting in a protcataclastic to ultracataclastic fabric (Pizzati et al., 2020; Nogueira et al., 2021) (Figures 5, 7 and 8). During the process, the grains experience internal fracturing. These fractures can display intra- or transgranular fracture styles (Figure 10C) (Aydin & Johnson, 1978; Balsamo & Storti, 2010; Fossen et al., 2018; Pizzati et al., 2020).

Pre-existing cleavage and fracture planes in K-feldspars, zeolites, pyroxenes, and amphiboles (Figures 5, 7 and 8) facilitate fragmentation and a formation of finer matrix (Dinwiddie et al., 2006; Cavailhes & Rotevatn, 2018; Fossen et al., 2018; Pizzati et al., 2020; Leroy et al., 2023).

Angular grains with sharp edges, particularly in K-feldspars, pyroxenes, and amphiboles (Figures 8D and 10C), contribute to the formation of microfaults (Figure 10C). These findings align with Dinwiddie et al. (2012), who observed microfractures parallel to cleavages and a fine matrix around crystals. Cataclasis further aligns grains and reduces porosity along the DBs.

Phillipsite grains exhibit intragranular tensile fractures (Figures 7D and 8E, 8F), resulting in isolated fragments locally sealed. This process likely reflects interactions between the rock and environmental fluids (Parry et al., 2004). Intragranular fracturing contributes to grain breakage and the formation of a finer-grained matrix (Sibson, 1977; Balsamo et al., 2010).

Unlike other studies on DBs in volcanoclastic rocks (e.g., Cavailhes & Rotevatn, 2018; Leroy et al., 2023), the zeolite, in this case, plays a significant role in deformation, acting as the weak phase. It undergoes greater deformation, leading to the formation of ultraclastic textures in some instances, concentrating strain, and facilitating sliding deformation, similar to the behavior of volcanic glass reported by Cavailhes & Rotevatn (2018). In contrast, the strong phase is composed of minerals such as K-feldspar, pyroxene, and amphibole, which form the most resistant portion of the DB.

The cataclastic flow phase is associated with the extensional stress field recorded from the Middle Pleistocene to the present. The NW–SE-oriented shortening stress is responsible for the right-lateral kinematics observed along the VTFZ (Barão et al., 2020), that promote the development of DBs and conjugate pair geometries. Also, this phase it may be influenced by ongoing magmatic activity at the Paredão Volcano (Pires et al., 2016; Pasqualon et al., 2019).

6. CONCLUSIONS

Examining the structures in both outcrops and thin sections of the Paredão Volcano on Trindade Island provides valuable insights into the structural evolution, kinematics, and deformation mechanisms that contributed to the formation of DBs in the pyroclastic rocks. The following conclusions can be drawn:

1. The initial stage of the volcanic system involved phreatomagmatic, Strombolian, and Hawaiian eruptions, producing flat, layered pyroclastic deposits. Subsequent fracturing, likely linked to volcanic collapse and VTFZ-related stress, developed radial patterns around the caldera. These fractures enabled hydrothermal alteration of lapilli-tuff through interaction with magmatic fluids and seawater, leading to a zeolitization process;
2. Zeolitization of lapilli-tuffs is attributed to the interplay between post-volcanic hydrothermal fluids and seawater. This interaction establishes a complex hydrogeological system within the rocks of the Paredão Volcano;
3. Deformation is primarily governed by granular flow as the dominant mechanism. This stage is characterized by subordinated fragmentation and rotation of crystal grains, which produce angular fragments in response to elevated fluid pressure;
4. Following the granular flow phase, cataclastic flow becomes the dominant deformation mechanism. This is evidenced by crystal fragmentation and the development of a fine-grained matrix within the main deformation zone, where observed

cataclastic to ultracataclastic textures. This results in the formation of a cataclastic fabric, accompanied by a reduction in pore size within the pyroclastic rocks along the DBs;

5. The process of cataclasis is strongly influenced by the mineralogical composition and occurs preferentially along cleavages or pre-existing microfractures. This phenomenon is particularly pronounced in minerals such as pyroxenes, K-feldspar, and amphiboles, where deformation is primarily associated with the development of fractures;
6. The zeolite fabric appears to be associated with the weak phase of deformation, acting as a secondary contributor to the development of DBs.

ACKNOWLEDGMENTS

This paper is part of L.M.B.'s PhD thesis developed within the PPGeol-UFPR. We gratefully acknowledge CNPq for financial support (projects 557299/05-5, 557141/2009-5, and 442865/2015-5), CAPES for the scholarship (88882382075/2019-01), and the Petrobras project "Controles de Trapas Estratigráficas Asociadas a Sistemas Turbidíticos" (nº 23075.075111/2022-15).

We thank the Brazilian Navy for logistical support during fieldwork, as well as the LABAP, LECOST, and iLAMIR laboratories for providing essential infrastructure. We are also grateful to the Geological Survey of Finland (GTK) and the Laboratory of Process Mineralogy for conducting key analyses and offering technical support, with special thanks to Akseli Torppa and Hannu T. Makkonen for their invaluable assistance.

R.J.A. acknowledges support as a CNPq research fellow (PQ 302913/2018-1). We extend our appreciation to PPGeol-UFPR for their ongoing support.

Finally, we thank Professors David L. Vasconcelos, Anderson Costa, and the anonymous reviewer for their valuable contributions. This manuscript benefited from the assistance of artificial intelligence (AI) tools for textual review and language refinement.

REFERENCES

- Adam, J., Urai, J. L., Wieneke, B., Oncken, O., Pfeiffer, K., Kukowski, N., Lohrmann, J., Hoth, S., van der Zee, W., & Schmatz, J. (2005). Shear localization and strain distribution during tectonic faulting - New insights from granular-flow experiments and high-resolution optical image correlation techniques. *Journal of Structural Geology*, 27(2), 283-301. <http://doi.org/10.1016/j.jsg.2004.08.008>.
- Alikarami, R., Torabi, A., Kolyukhin, D., & Skurtveit, E. (2013). Geostatistical relationships between mechanical and petrophysical properties of deformed sandstone. *International Journal of Rock Mechanics and Mining Sciences*, 63, 27-38. <http://doi.org/10.1016/j.ijrmms.2013.06.002>.
- Almeida, F. (2006). Ilhas oceânicas brasileiras e suas relações com a tectônica atlântica. *Terrae Didática*, 2(1), 3-18. <http://doi.org/10.20396/tdd.v2i1.8637462>.
- Almeida, F. F. M. (1961). *Geologia e Petrologia da Ilha de Trindade*. Rio de Janeiro: Divisão de Geologia e Mineralogia.
- Alves, E. C., Maia, M., Sichel, S. E., & Campos, C. M. P. (2006). Zona de fratura de Vitória-Trindade no Oceano Atlântico sudeste e suas implicações tectônicas. *Revista Brasileira de Geofísica*, 24(1), 117-127. <http://doi.org/10.1590/S0102-261X2006000100009>.
- Alves, E. C., Araújo, R. S., Ramos, E. C., Maia, M., Santos, A. C., & Hackspacher, P. C. (2022). Ocean fracture zones: Their evolution and impact on tectonic and magmatism of the South and Southeast Brazilian continental margin. In A. C. Santos & P. C. Hackspacher (Eds.), *Meso-cenozoic Brazilian offshore magmatism* (pp. 47-94). London: Academic Press.
- Antonellini, M., & Aydin, A. (1995). Effect of faulting on fluid-flow geometry and spatial-distribution. *AAPG Bulletin*, 79(5), 642-671. <http://doi.org/10.1306/8D2B1B60-171E-11D7-8645000102C1865D>.
- Aydin, A. (1978). Small faults formed as deformation bands in sandstone. *Pure and Applied Geophysics*, 116(4-5), 913-930. <http://doi.org/10.1007/BF00876546>.
- Aydin, A., & Johnson, M. (1978). Development of faults as zones of deformation bands and slip surfaces in sandstone. *Pure and Applied Geophysics*, 116(4-5), 931-942. <http://doi.org/10.1007/BF00876547>.
- Ballas, G., Soliva, R., Sizun, J., Benedicto, A., Cavailhes, T., & Raynaud, S. (2012). The importance of the degree of cataclasis in shear bands for fluid flow in porous sandstone. *AAPG Bulletin*, 96(11), 2167-2186. <http://doi.org/10.1306/04051211097>.
- Balsamo, F., & Storti, F. (2010). Grain size and permeability evolution of soft-sediment extensional sub-seismic and seismic fault zones in high-porosity sediments from the Croton basin, southern Apennines, Italy. *Marine and Petroleum Geology*, 27(4), 822-837. <http://doi.org/10.1016/j.marpetgeo.2009.10.016>.
- Balsamo, F., Storti, F., Salvini, F., Silva, A. T., & Lima, C. C. (2010). Structural and petrophysical evolution of extensional fault zones in low-porosity, poorly lithified sandstones of the Barreiras Formation, NE Brazil. *Journal of Structural Geology*, 32(11), 1806-1826. <http://doi.org/10.1016/j.jsg.2009.10.010>.
- Barão, L. M., Trzaskos, B., Angulo, R. J., Souza, M. C., Avelar, F., Garcia, M. H., & Oliveira, L. S. (2018). Feições estruturais observadas nas ilhas de Trindade e Fernando de Noronha e sua relação com tectônica atual. In 49º Congresso Brasileiro de Geologia. Rio de Janeiro: Sociedade Brasileira de Geologia.
- Barão, L. M., Trzaskos, B., Angulo, R. J., Souza, M. C., Daufenbach, H. F., Santos, F. A., & Vasconcelos, E. M. G. (2020). Deformational structures developed in volcanic sequences as a product of tectonic adjustments in the South Atlantic Ocean. *Journal of South American Earth Sciences*, 104, 102812. <http://doi.org/10.1016/j.jsames.2020.102812>.
- Bense, V. F., & Van Balen, R. (2004). The effect of fault relay and clay smearing on groundwater flow patterns in the Lower Rhine Embayment. *Basin Research*, 16(3), 397-411. <http://doi.org/10.1111/j.1365-2117.2004.00238.x>.
- Bemis, S. P., Mickelthwaite, S., Turner, D., James, M. R., Akciz, S. T., Thiele, S., & Bangash, H. A. (2014). Ground-based and UAV-Based photogrammetry: A multi scale, high-resolution mapping tool for structural geology and paleoseismology. *Journal of Structural Geology*, 69, 163-178. <http://doi.org/10.1016/j.jsg.2014.10.007>.
- Berge, R. L., Gasda, S. E., Keilegavlen, E., & Sandve, T. H. (2022). Impact of deformation bands on fault-related fluid flow in field-scale simulations. *International Journal of Greenhouse Gas Control*, 119, 103729. <http://doi.org/10.1016/j.ijggc.2022.103729>.
- Bonato, J., Tognoli, F. M. W., Nogueira, F. C. C., Miranda, T. S., & Inocencio, L. C. (2022). The use of network topology to assess connectivity of deformation bands in sandstone: A quantitative approach based on digital outcrop models. *Journal of Structural Geology*, 161, 104682. <http://doi.org/10.1016/j.jsg.2022.104682>.
- Bongiolo, E. M., Pires, G. L. C., Gerales, M. C., Santos, A. C., & Neumann, R. (2015). Geochemical modeling and Nd-Sr data links nephelinite-phonolite successions and xenoliths of Trindade Island (South Atlantic Ocean, Brazil). *Journal of Volcanology and Geothermal Research*, 306, 58-73. <http://doi.org/10.1016/j.jvolgeores.2015.10.002>.
- Cavailhes, T., & Rotevatn, A. (2018). Deformation bands in volcanoclastic rocks: Insights from the Shihtiping tuffs, Coastal Range of Taiwan. *Journal of Structural Geology*, 113, 155-175. <http://doi.org/10.1016/j.jsg.2018.06.004>.
- Christidis, G. E. (2001). Formation and growth of smectites in bentonites: A case study from Kimolos Island, Aegean, Greece. *Clays and Clay Minerals*, 49(3), 204-215. <http://doi.org/10.1346/CCMN.2001.0490303>.
- Chuhan, F. A., Kjeldstad, A., Bjørlykke, K., & Høeg, K. (2002). Porosity loss in sand by grain crushing - Experimental evidence and relevance to reservoir quality. *Marine and Petroleum Geology*, 19(1), 39-53. [http://doi.org/10.1016/S0264-8172\(01\)00049-6](http://doi.org/10.1016/S0264-8172(01)00049-6).
- Chung, C. C., Chen, C. T., & Lu, C. Y. (2023). Quantitative analyses of deformation band occurrence and host rock properties in pyroclastic rocks of eastern Taiwan. *Journal of Structural Geology*, 173, 104910. <http://doi.org/10.1016/j.jsg.2023.104910>.

- Cilona, A., Baud, P., Tondi, E., Agosta, F., Vinciguerra, S., Rustichelli, A., & Spiers, C. J. (2012). Deformation bands in porous carbonate grainstones: Field and laboratory observations. *Journal of Structural Geology*, 45, 137-157. <http://doi.org/10.1016/j.jsg.2012.04.012>.
- Cimarelli, C., & De Rita, D. (2006). Structural evolution of the Pleistocene Cimini trachytic volcanic complex (Central Italy). *Bulletin of Volcanology*, 68(6), 538-548. <http://doi.org/10.1007/s00445-005-0028-3>.
- Cladouhos, T. T. (1999). Shape preferred orientations of survivor grains in fault gouge. *Journal of Structural Geology*, 21(4), 419-436. [http://doi.org/10.1016/S0191-8141\(98\)00123-0](http://doi.org/10.1016/S0191-8141(98)00123-0).
- De Rita, D., Funicello, R., Rossi, U., & Sposato, A. (1983). Structure and evolution of the Sacrofano-Baccano caldera, Sabatini volcanic complex, Rome. *Journal of Volcanology and Geothermal Research*, 17(1-4), 219-236. [http://doi.org/10.1016/0377-0273\(83\)90069-0](http://doi.org/10.1016/0377-0273(83)90069-0).
- Del Sole, L., & Antonellini, M. (2019). Microstructural, petrophysical, and mechanical properties of compactive shear bands associated to calcite cement concretions in arkose sandstone. *Journal of Structural Geology*, 126, 51-68. <http://doi.org/10.1016/j.jsg.2019.05.007>.
- Del Sole, L., Antonellini, M., & Calafato, A. (2020). Characterization of sub-seismic resolution structural diagenetic heterogeneities in porous sandstones: Combining ground-penetrating radar profiles with geomechanical and petrophysical in situ measurements (Northern Apennines, Italy). *Marine and Petroleum Geology*, 117, 104375. <http://doi.org/10.1016/j.marpetgeo.2020.104375>.
- Dimmen, V., Rotevatn, A., Peacock, D. C. P., Nixon, C. W., & Nærlund, K. (2017). Quantifying structural controls on fluid flow: Insights from carbonate-hosted fault damage zones on the Maltese Islands. *Journal of Structural Geology*, 101, 43-57. <http://doi.org/10.1016/j.jsg.2017.05.012>.
- Dinwiddie, C. L., Bradbury, K. K., McGinnis, R. N., Fedors, R. W., & Ferrill, D. A. (2006). Fault zone deformation overprints permeability of nonwelded ignimbrite: Chalk cove fault, Bishop Tuff, Bishop, California. *Vadose Zone Journal*, 5(2), 610-627. <http://doi.org/10.2136/vzj2005.0062>.
- Dinwiddie, C. L., Bradbury, K. K., McGinnis, R. N., Stillman, D. E., & Ferrill, D. A. (2012). Hydrogeologic heterogeneity of faulted and fractured Glass Mountain bedded tuffaceous sediments and ash-fall deposits: The Crucifix site near Bishop, California. *Lithosphere*, 4(1), 40-62. <http://doi.org/10.1130/L179.1>.
- Etame, J., Suh, C. E., Gerard, M., & Bilong, P. (2012). Phillipsite formation in nephelinitic rocks in response to hydrothermal alteration at Mount Etinde, Cameroon. *Chemie der Erde*, 72(1), 31-37. <http://doi.org/10.1016/j.chemer.2011.08.002>.
- Evans, J. P., & Bradbury, K. K. (2004). Faulting and fracturing of nonwelded Bishop Tuff, Eastern California: Deformation mechanisms in very porous materials in the vadose zone. *Vadose Zone Journal*, 3(2), 602-623. <http://doi.org/10.2136/vzj2004.0602>.
- Exner, U., & Tscheegg, C. (2012). Preferential cataclastic grain size reduction of feldspar in deformation bands in poorly consolidated arkosic sands. *Journal of Structural Geology*, 43(1), 63-72. <http://doi.org/10.1016/j.jsg.2012.08.005>. PMID:26523078.
- Farrell, N. J. C., Healy, D., & Taylor, C. W. (2014). Anisotropy of permeability in faulted porous sandstones. *Journal of Structural Geology*, 63, 50-67. <http://doi.org/10.1016/j.jsg.2014.02.008>.
- Ferrari, L. A., & Riccomini, C. (1999). Campo de Esforços Plio-Pleistocênico na Ilha da Trindade (Oceano Atlântico Sul, Brasil) e sua relação com a tectônica regional. *Revista Brasileira de Geociências*, 29(2), 195-202. <http://doi.org/10.25249/0375-7536.199929195202>.
- Ferreira, T., & Rasband, W. (2012). *ImageJ User Guide*. Bethesda: National Institutes of Health.
- Fossen, H., Schultz, A. R., Shipton, Z. K., & Mair, K. (2007). Deformation bands in sandstone: A review. *Journal of the Geological Society*, 164(4), 755-769. <http://doi.org/10.1144/0016-76492006-036>.
- Fossen, H., Soliva, R., Ballas, G., Trzaskos, B., Cavalcante, C., & Schultz, R. A. (2018). A review of deformation bands in reservoir sandstones: Geometries, mechanisms and distribution. *Geological Society Special Publication*, 459, 9-33. <http://doi.org/10.1144/SP459.4>.
- Freitas, R. B. R. M., Nogueira, F. C. C., Vasconcelos, D. L., Honório, G. B., Nicchio, M. A., Stohler, R. C., & Souza, J. A. B. (2023). 3D topological analysis in deformation bands: Insights for structural characterization and impact on permeability. *Journal of Structural Geology*, 176, 104959. <http://doi.org/10.1016/j.jsg.2023.104959>.
- Ghiara, M. R., & Petti, C. (1996). Chemical alteration of volcanic glasses and related control by secondary minerals: Experimental studies. *Aquatic Geochemistry*, 1(4), 329-354. <http://doi.org/10.1007/BF00702738>.
- Gibson, S. A., Thompson, R. N., & Day, J. A. (2006). Timescales and mechanisms of plume-lithosphere interactions: 40Ar/39Ar geochronology and geochemistry of alkaline igneous rocks from the Paraná-Etendeka large igneous province. *Earth and Planetary Science Letters*, 251(1-2), 1-17. <http://doi.org/10.1016/j.epsl.2006.08.004>.
- Godelistas, A., Gamaletsos, P., & Roussos-Kotis, M. (2010). Mordenite-bearing tuffs from Prassa quarry, Kimolos island, Greece. *European Journal of Mineralogy*, 22(6), 797-811. <http://doi.org/10.1127/0935-1221/2010/0022-2058>.
- Grove, C., & Jerram, D. A. (2011). JPOR: An ImageJ macro to quantify total optical porosity from blue-stained thin sections. *Computers & Geosciences*, 37(11), 1850-1859. <http://doi.org/10.1016/j.cageo.2011.03.002>.
- Gudmundsson, A. (2006). How local stresses control magma-chamber ruptures, dyke injections, and eruptions in composite volcanoes. *Earth-Science Reviews*, 79(1-2), 1-31. <http://doi.org/10.1016/j.earscirev.2006.06.006>.
- Hartnady, C. J. H., & Le Roex, A. P. (1985). Southern Ocean hotspot tracks and the Cenozoic absolute motion of the African, Antarctic, and South American plates. *Earth and Planetary Science Letters*, 75(2-3), 245-257. [http://doi.org/10.1016/0012-821X\(85\)90106-2](http://doi.org/10.1016/0012-821X(85)90106-2).
- Hay, R. L. (1977). Geology of zeolites in sedimentary rocks. *Reviews in Mineralogy, Mineralogical Society of America*, 4, 53-64. <http://doi.org/10.2138/rmg.2001.45.6>.
- Hawkesworth, C., Kelley, S., Turner, S., Roex, A. L. E., & Storey, B. (1999). Mantle processes during Gondwana break-up and dispersal. *Journal of African Earth Sciences*, 28(1), 239-261. [http://doi.org/10.1016/S0899-5362\(99\)00026-3](http://doi.org/10.1016/S0899-5362(99)00026-3).
- Hernandez, J. E. G., Notario del Pino, J. S., Gonzalez Martin, M. M., Hernan Reguera, F., & Losada, J. A. R. (1993). Zeolites in pyroclastic deposits in southeastern Tenerife (Canary Islands). *Clays and Clay Minerals*, 41(5), 521-526. <http://doi.org/10.1346/CCMN.1993.0410501>.
- Jha, M. K., Mahapatra, S., & Mohan, C. (2019). Infiltration characteristics of lateritic vadose zones: Field experiments and modeling. *Soil & Tillage Research*, 187, 219-234. <http://doi.org/10.1016/j.still.2018.12.007>.
- Kong, L., Ostadhassan, M., Hou, X., Mann, M., & Li, C. (2019). Microstructure characteristics and fractal analysis of 3D-printed sandstone using micro-CT and SEM-EDS. *Journal of Petroleum Science Engineering*, 175, 1039-1048. <http://doi.org/10.1016/j.petrol.2019.01.050>.
- Krolow, P., Jantschke, A., Gilbricht, S., Niiranen, K., & Seifert, T. (2019). Mineralogical imaging for characterization of the per geijer apatite iron ores in the Kiruna district, northern Sweden: A comparative study of mineral liberation analysis and raman imaging. *Minerals*, 9(9), 544. <http://doi.org/10.3390/min9090544>.
- Leroy, E., Cavailhes, T., Anguy, Y., Soliva, R., Rotevatn, A., & Gaborieau, C. (2023). Deformation bands and alteration in porous glass-rich volcanics: Insights from Milos, Greece. *Journal of Structural Geology*, 177, 104982. <http://doi.org/10.1016/j.jsg.2023.104982>.
- Mair, K., Frye, K. M., & Marone, C. (2002). Influence of grain characteristics on the friction of granular shear zones. *Journal of Geophysical Research: Solid Earth*, 107, ECV 4-1-ECV 4-9. <http://doi.org/10.1029/2001JB000516>.
- Marques, L. S., Ulbrich, M. N. C., Ruberti, E., & Tassinari, C. G. (1999). Petrology, geochemistry and Sm-Nd isotopes of the Trindade and Martin Vaz volcanic rocks (Southern Atlantic Ocean). *Journal of Volcanology Geothermal Research*, 93(3-4), 191-216. [http://doi.org/10.1016/S0377-0273\(99\)00111-0](http://doi.org/10.1016/S0377-0273(99)00111-0).
- Mateus, A. C. C., Varajão, A. F. D. C., Petit, S., Oliveira, F. S., & Schaefer, C. E. G. R. (2020). Mineralogical and geochemical signatures of Quaternary pyroclastic alterations at the volcanic Trindade Island, South Atlantic. *Journal of South American Earth Sciences*, 102, 102674. <http://doi.org/10.1016/j.jsames.2020.102674>.
- McGinnis, R. N., Morris, A. P., Ferrill, D. A., & Dinwiddie, C. L. (2009). Deformation analysis of tuffaceous sediments in the Volcanic Tableland near Bishop, California. *Lithosphere*, 1(5), 291-304. <http://doi.org/10.1130/L43.1>.

- Medeiros, W. E., Nascimento, A. F., Silva, A. F., Destro, N., & Demétrio, J. G. A. (2010). Evidence of hydraulic connectivity across deformation bands from field pumping tests: Two examples from Tucano Basin, NE Brazil. *Journal of Structural Geology*, 32(11), 1783-1791. <http://doi.org/10.1016/j.jsg.2009.08.019>.
- Mollema, P. N., & Antonellini, M. A. (1996). Compaction bands: A structural analog for anti-mode I cracks in aeolian sandstone. *Tectonophysics*, 267(1-4), 209-228. [http://doi.org/10.1016/S0040-1951\(96\)00098-4](http://doi.org/10.1016/S0040-1951(96)00098-4).
- Monteiro, L. G., Santos, A. C., Pires, G., Barão, L. M., Hackspacher, P. C., Santos, J. F., Biancini, R., Rocha-Júnior, E. R. V., Jeck, I. K., & Araujo, J. H. I. (2022). Trindade Island: Evolution of the geological knowledge. In A. C. Santos & P. C. Hackspacher (Eds.), *Meso-Cenozoic Brazilian Offshore Magmatism Geochemistry, Petrology, and Tectonics* (1st ed., Vol. 1, pp. 337-389). London: Elsevier. <http://doi.org/10.1016/B978-0-12-823988-9.00015-0>
- Motoki, K., Campos, T. F. C., Santos, A., Heilbron, M., Barão, L. M., Sichel, S., Ferrari, A., Fonseca, E., & Szatmari, P. (2024). Interpretation of high-resolution remote sensing data for plio-pleistocene tectonic structures studies in the Trindade Island volcanic building, South Atlantic Ocean, Brazil. In: Cengiz, M. & Karabulu, S (Eds.), *Formation and Evolution of Earth's Crust* (pp. 1-24). London: IntechOpen. <http://doi.org/10.5772/intechopen.113254>.
- Nicchio, M. A., Nogueira, F. C. C., Balsamo, F. J., Souza, J. A. B., Carvalho, B. R. B. M., & Bezerra, F. H. R. (2018). Development of cataclastic foliation in deformation bands in feldspar-rich conglomerates of the Rio do Peixe Basin, NE Brazil. *Journal of Structural Geology*, 107, 132-141. <http://doi.org/10.1016/j.jsg.2017.12.013>.
- Nicchio, A. M., Balsamo, F., Francisco, C., Aldega, L., Cesar, C., Pontes, C., Bezerra, F. H., Souza, J. A. B., Hilario, F., & Andr, J. (2023). The effect of fault-induced compaction on petrophysical properties of deformation bands in poorly lithified sandstones. *Journal of Structural Geology*, 166, 104758. <http://doi.org/10.1016/j.jsg.2022.104758>.
- Nogueira, F. C. C., Nicchio, M. A., Balsamo, F., Souza, J. A. B., Silva, I. V. L., Bezerra, F. H. R., Vasconcelos, D. L., & Carvalho, B. R. B. M. (2021). The influence of the cataclastic matrix on the petrophysical properties of deformation bands in arkosic sandstones. *Marine and Petroleum Geology*, 124, 104825. <http://doi.org/10.1016/j.marpetgeo.2020.104825>.
- Norini, G., Carrasco-Núñez, G., Corbo-Camargo, F., Lermo, J., Rojas, J. H., Castro, C., Bonini, M., Montanari, D., Corti, G., Moratti, G., Piccardi, L., Chavez, G., Zuluaga, M. C., Ramirez, M., & Cedillo, F. (2019). The structural architecture of the Los Humeros volcanic complex and geothermal field. *Journal of Volcanology and Geothermal Research*, 381, 312-329. <http://doi.org/10.1016/j.jvolgeores.2019.06.010>.
- Okubo, C., Schultz, R. A., Chan, M. A., & Komatsu, G. (2009). Deformation band clusters on Mars and implications for subsurface fluid flow. *Bulletin of the Geological Society of America*, 121(3-4), 474-482. <http://doi.org/10.1130/B26421.1>.
- Parry, W. T., Chan, M. A., & Beitler, B. (2004). Chemical bleaching indicates episodes of fluid flow in deformation bands in sandstone. *AAPG Bulletin*, 88(2), 175-191. <http://doi.org/10.1306/09090303034>.
- Pasqualon, N. G., Lima, E. F., Scherer, C. M. S., Rossetti, L. M. M., & Luz, F. R. (2019). Lithofacies association and stratigraphy of the Paredão Volcano, Trindade Island, Brazil. *Journal of Volcanology and Geothermal Research*, 380, 48-63. <http://doi.org/10.1016/j.jvolgeores.2019.05.011>.
- Pires, G. L. C., Bongioiolo, E. M., Gerales, M. C., Renac, C., Santos, A. C., Jourdan, F., & Neumann, R. (2016). New ⁴⁰Ar/³⁹Ar ages and revised ⁴⁰K/⁴⁰Ar* data from nephelinitic-phonolitic volcanic successions of the Trindade Island (South Atlantic Ocean). *Journal of Volcanology and Geothermal Research*, 327, 531-538. <http://doi.org/10.1016/j.jvolgeores.2016.09.020>.
- Pizzati, M., Balsamo, F., & Storti, F. (2020). Displacement-dependent microstructural and petrophysical properties of deformation bands and gouges in poorly lithified sandstone deformed at shallow burial depth (Crotone Basin, Italy). *Journal of Structural Geology*, 137, 104069. <http://doi.org/10.1016/j.jsg.2020.104069>.
- Queiroz, G. L., Salamuni, E., & Nascimento, E. R. (2014). AzimuthFinder: Ferramenta para a extração de dados e apoio na análise estrutural. *Geologia USP - Série Científica*, 14, 69-80.
- Ramalho, R. S., Quartau, R., Trenhaile, A. S., Mitchell, N. C., Woodroffe, C. D., & Ávila, S. A. (2013). Coastal evolution on volcanic oceanic islands: A complex interplay between volcanism, erosion, sedimentation, sea-level change and biogenic production. *Earth-Science Reviews*, 127, 140-170. <http://doi.org/10.1016/j.earscirev.2013.10.007>.
- Rawling, G. C., & Goodwin, L. B. (2003). Cataclasis and particulate flow in faulted, poorly lithified sediments. *Journal of Structural Geology*, 25(3), 317-331. [http://doi.org/10.1016/S0191-8141\(02\)00041-X](http://doi.org/10.1016/S0191-8141(02)00041-X).
- Rego, C. A. Q., Quaresma, G. O. A., Santos, A. C., Mohriak, W. U., Jesus, J. V. M., & Rodrigues, S. W. O. (2021). Davis Bank geodynamic context, South Atlantic Ocean: Insights into the Vitória-Trindade Ridge evolution. *Journal of South American Earth Sciences*, 112, 103620. <http://doi.org/10.1016/j.jsames.2021.103620>.
- Ribeiro, C. V., Patrício, R. L., & Hackspacher, P. C. (2019). Evolução tectono-magmática da Ilha de Trindade, Atlântico Sul. In 28º *Simpósio de Geologia Do Nordeste*. São Paulo: Sociedade Brasileira de Geologia.
- Robert, C., & Goffé, B. (1993). Zeolitization of basalts in subaqueous freshwater settings: Field observations and experimental study. *Geochimica et Cosmochimica Acta*, 57(15), 3597-3612. [http://doi.org/10.1016/0016-7037\(93\)90142-J](http://doi.org/10.1016/0016-7037(93)90142-J).
- Rodrigues, M. C. N. L., Trzaskos, B., & Lopes, A. (2015). Influence of deformation bands on sandstone porosity: A case study using three-dimensional microtomography. *Journal of Structural Geology*, 72, 96-110. <http://doi.org/10.1016/j.jsg.2015.01.003>.
- Santos, F. A., Zuquette, L. V., Ângulo, R. F., Souza, M. C., Talamini, A. A., Barão, L. M., Daufenbach, H. F., & Garcia, M. H. (2025). Erosion processes and gravitational mass movements on Trindade Island, Brazil (South Atlantic Ocean). *Geomorphology*, 469, 109516. <http://doi.org/10.1016/j.geomorph.2024.109516>.
- Schneider, C. A., Rasband, W. S., & Eliceiri, K. W. (2012). NIH Image to ImageJ: 25 years of image analysis. *Nature Methods*, 9(7), 671-675. <http://doi.org/10.1038/nmeth.2089>.
- Shipton, Z. K., Evans, J. P., Robeson, K., Forster, C. B., & Snelgrove, S. (2002). Structural heterogeneity and permeability in faulted eolian sandstone: Implications for subsurface modelling of faults. *AAPG Bulletin*, 86, 863-883. <http://doi.org/10.1306/61EEDBC0-173E-11D7-8645000102C1865D>.
- Sibson, R. H. (1977). Fault rocks and fault mechanisms. *Journal of the Geological Society*, 133(3), 191-213. <http://doi.org/10.1144/gsjgs.133.3.0191>.
- Siebel, W., Becchio, R., Volker, F., Hansen, M. A. F., Viramonte, J., Trumbull, R. B., Haase, G., & Zimmer, M. (2000). Trindade and Martin Vaz Islands, South Atlantic: Isotopic (Sr, Nd, Pb) and trace element constraints on plume related magmatism. *Journal of South American Earth Sciences*, 13(1-2), 79-103. [http://doi.org/10.1016/S0895-9811\(00\)00015-8](http://doi.org/10.1016/S0895-9811(00)00015-8).
- Silva, M. E., Nogueira, F. C. C., Pérez, Y. A. R., Vasconcelos, D. L., Stohler, R. C., Sanglard, J. C. D., Balsamo, F., Bezerra, F. H. R., Carvalho, B. R. B. M., & Souza, J. A. B. (2022). Permeability modeling of a basin-bounding fault damage zone in the Rio do Peixe Basin, Brazil. *Marine and Petroleum Geology*, 135, 105409. <http://doi.org/10.1016/j.marpetgeo.2021.105409>.
- Soliva, R., Ballas, G., Fossen, H., & Philit, S. (2016). Tectonic regime controls clustering of deformation bands in porous sandstone. *Geology*, 44(6), 423-426. <http://doi.org/10.1130/G37585.1>.
- Souza, D. H. S. S., Nogueira, F. C. C., Vasconcelos, D. L., Torabi, A., Souza, J. A. B., Nicchio, M. A., Pérez, Y. A. R., & Balsamo, F. (2021). Growth of cataclastic bands into a fault zone: A multiscale process by microcrack coalescence in sandstones of Rio do Peixe Basin, NE Brazil. *Journal of Structural Geology*, 146, 104315. <http://doi.org/10.1016/j.jsg.2021.104315>.
- Souza, F. M., Gomes, I. F., Nogueira, F. C. C., Vasconcelos, D. L., Canabarro, B., Souza, J. A. B., Guimarães, L. J. N., & Beserra, L. B. S. (2022). 2D modeling and simulation of deformation bands' effect on fluid flow: Implications for hydraulic properties in siliciclastic reservoirs. *Journal of Structural Geology*, 158, 104581. <http://doi.org/10.1016/j.jsg.2022.104581>.
- Speciale, P. A., Tokle, L., & Behr, W. M. (2022). Feldspar and orthopyroxene piezometers constrained using quartz-feldspar and olivine-orthopyroxene mineral pairs from natural mylonites. *Journal of Structural Geology*, 154, 104495. <http://doi.org/10.1016/j.jsg.2021.104495>.
- Stohler, R. C., Nogueira, F. C. C., Mello, C. L., & Souza, J. A. B. (2022). 3D numerical modelling and simulation of the impact of fault zones on fluid flow in sandstones of the Rio do Peixe Basin, NE Brazil. *Petroleum Geoscience*, 28(4), petgeo2022-024. <http://doi.org/10.1144/petgeo2022-024>.

- Szatmari P. & Mohriak W. U. (1995). Plate model of post-breakup tectono-magmatic activity in SE Brazil and the adjacent Atlantic. In *Anais do Simpósio Nacional de Estudos Tectônicos* (pp. 213-214). São Paulo: Sociedade Brasileira de Geologia.
- Torabi, A. (2014). Cataclastic bands in immature and poorly lithified sandstone, examples from Corsica, France. *Tectonophysics*, 630, 91-102. <http://doi.org/10.1016/j.tecto.2014.05.014>.
- Torabi, A., Balsamo, F., Nogueira, F. C. C., Vasconcelos, D. L., Silva, A. C. E., Bezerra, F. H. R., & Souza, J. A. B. (2021). Variation of thickness, internal structure and petrophysical properties in a deformation band fault zone in siliciclastic rocks. *Marine and Petroleum Geology*, 133, 105297. <http://doi.org/10.1016/j.marpetgeo.2021.105297>.
- Tondi, E., Antonellini, M., Aydin, A., Marchegiani, L., & Cello, G. (2006). The role of deformation bands, stylolites and sheared stylolites in fault development in carbonate grainstones of Majella Mountain, Italy. *Journal of Structural Geology*, 28(3), 376-391. <http://doi.org/10.1016/j.jsg.2005.12.001>.
- Ulrich, S., Hobbs, B. E., Ord, A., & Schulmann, K. (2020). The relative strengths of deforming mineral phase assemblages: Geometrically necessary deformation mechanisms. *Journal of Structural Geology*, 137, 104056. <http://doi.org/10.1016/j.jsg.2020.104056>.
- Valdivia, M. R. (2022). Síntesis hidrotermal de zeolitas a partir de ceniza volcánica mediante tratamiento alcalino y su potencial aplicación en la remoción de NH₄⁺, Pb²⁺, Zn²⁺ y Mn²⁺. *Matéria*, 27(1), e13132. <http://doi.org/10.1590/s1517-707620220001.1332>.
- Wilson, J. E., Goodwin, L. B., & Lewis, C. J. (2003). Deformation bands in nonwelded ignimbrites: Petrophysical controls on fault-zone deformation and evidence of preferential fluid flow. *Geology*, 31(10), 837-840. <http://doi.org/10.1130/G19667R.1>.
- Wilson, J. E., Goodwin, L. B., & Lewis, C. (2006). Diagenesis of deformation band faults: Record and mechanical consequences of vadose zone flow and transport in the Bandelier Tuff, Los Alamos, New Mexico. *Journal of Geophysical Research*, 111(B9), 1-19. <http://doi.org/10.1029/2005JB003892>.
- Wilson, P. I. R., Wilson, R. W., Sanderson, D. J., Jarvis, I., & McCaffrey, K. J. W. (2021). Analysis of deformation bands associated with the Trachyte Mesa intrusion, Henry Mountains, Utah: Implications for reservoir connectivity and fluid flow around sill intrusions. *Solid Earth*, 12(1), 95-117. <http://doi.org/10.5194/se-12-95-2021>.
- Zuluaga, L. F., Fossen, H., & Rotevatn, A. (2014). Progressive evolution of deformation band populations during Laramide fault-propagation folding: Navajo Sandstone, San Rafael monocline, Utah, U.S.A. *Journal of Structural Geology*, 68, 66-81. <http://doi.org/10.1016/j.jsg.2014.09.008>.

ARTICLE INFORMATION

Manuscript ID: BJGEO-2025-0013. Received on: 23 MAY 2025. Approved on: 21 JUL 2025.


How to cite: Barão, L. M., Trzaskos, B., Lagoeiro, L. E., Laukkanen, J., Salvador, D. A., Daufenbach, H. F., Pasqualon, N. G., Souza, M. C., & Angulo, R. J. Cataclastic deformation bands affecting alkaline volcanoclastics along an emerged island in oceanic fracture zone: the Paredão Volcano, Trindade Island. *Braz. J. Geol.* (2025), 55:e20250013. <https://doi.org/10.1590/2317-4889e20250013>

LMB: Conceptualization (Lead), Data curation (Lead), Formal analysis (Lead), Investigation (Lead), Methodology (Lead), Resources (Lead), Writing - original draft (Lead), Writing - review & editing (Lead). BT: Data curation (Equal), Methodology (Equal), Project administration (Lead), Supervision (Lead), Validation (Equal), Visualization (Equal), Writing - review & editing (Lead). LEL: Methodology (Supporting), Supervision (Supporting), Validation (Supporting), Writing - review & editing (Supporting). JL: Investigation (Supporting), Methodology (Supporting), Resources (Supporting), Software (Supporting). DAS: Investigation (Equal), Methodology (Equal), Resources (Equal), Software (Equal), Writing - original draft (Equal), Writing - review & editing (Equal). HFD: Data curation (Equal), Formal analysis (Equal), Investigation (Supporting), Methodology (Equal), Writing - original draft (Equal). NGP: Investigation (Supporting), Methodology (Equal), Writing - original draft (Equal). MCS: Conceptualization (Equal), Funding acquisition (Lead), Investigation (Supporting), Project administration (Lead), Resources (Lead), Writing - original draft (Equal). RJA: Funding acquisition (Lead), Investigation (Supporting), Methodology (Supporting), Project administration (Lead), Resources (Lead), Writing - original draft (Equal).

Conflict of interest: No conflicts of interest declared concerning the publication of this article.

Data availability statement: The entire dataset supporting the results of this study has been published in the article and in the “Supplementary Materials” section, which belongs to the paper.

SCIENTIFIC EDITOR: Carlos Grohmann 

ASSOCIATE EDITOR: Andres Folguera 

Supplementary Material

Supplementary material accompanies this paper.

Supplementary Material 1 - EDX spectrum for matrix and zeolite.

Supplementary Material 2 - Raman spectrum of the zeolite mineral, phillipsite. The spectrum below (black) is from the studied sample. The upper one (blue) is from RRUFF-database. The matching percentage is 98%. The laser wavelength was 532 nm.

This material is available as part of the online article from <https://doi.org/10.1590/2317-4889e20250013>